Assembly and Molecular Architecture of the Phosphoinositide 3-Kinase p85α Homodimer*

Jaclyn LoPiccolo[‡1], **Seung Joong Kim**[§1], **Yi Shi**[¶], **Bin Wu**[‖], **Haiyan Wu**[‡], **Brian T. Chait**[¶], **Robert H. Singer**[‖], **Andrej Sali**[§], **Michael Brenowitz**[**2], **Anne R. Bresnick**[**3], **and Jonathan M. Backer**[‡**4]

From the ‡Department of Molecular Pharmacology, **Department of Biochemistry, ‖Department of Anatomy and Structural Biology, Albert Einstein College of Medicine, Bronx, New York 10461, the §Department of Bioengineering and Therapeutic Sciences, Department of Pharmaceutical Chemistry, and California Institute for Quantitative Biosciences, University of California, San Francisco, San Francisco, California 94158, and the ¶Laboratory of Mass Spectrometry and Gaseous Ion Chemistry, The Rockefeller University, New York, New York 10065

Background: The class IA PI 3-kinase regulatory subunit p85α dimerizes by mechanisms not fully understood.
Results: p85α dimerization is driven by intermolecular interactions at both its N and C termini. A structural model of the p85α dimer reveals conformational diversity.
Conclusion: p85α dimerization is poised to link the heterologous assemblies that regulate PI3K signaling.
Significance: The p85α dimer is a dynamic participant in PI3K signaling.

Phosphoinositide 3-kinases (PI3Ks) are a family of lipid kinases that are activated by growth factor and G-protein-coupled receptors and propagate intracellular signals for growth, survival, proliferation, and metabolism. p85α, a modular protein consisting of five domains, binds and inhibits the enzymatic activity of class IA PI3K catalytic subunits. Here, we describe the structural states of the p85α dimer, based on data from *in vivo* and *in vitro* solution characterization. Our *in vitro* assembly and structural analyses have been enabled by the creation of cysteine-free p85α that is functionally equivalent to native p85α. Analytical ultracentrifugation studies showed that p85α undergoes rapidly reversible monomer-dimer assembly that is highly exothermic in nature. In addition to the documented SH3-PR1 dimerization interaction, we identified a second intermolecular interaction mediated by cSH2 domains at the C-terminal end of the polypeptide. We have demonstrated *in vivo* concentration-dependent dimerization of p85α using fluorescence fluctuation spectroscopy. Finally, we have defined solution conditions under which the protein is predominantly monomeric or dimeric, providing the basis for small angle x-ray scattering and chemical cross-linking structural analysis of the discrete dimer. These experimental data have been used for the integrative structure determination of the p85α dimer. Our study provides new insight into the structure and assembly of the p85α homodimer and suggests that this protein is a highly dynamic molecule whose conformational flexibility allows it to transiently associate with multiple binding proteins.

p85α (PIK3R1) is one of five regulatory subunits that inhibit and stabilize the p110 catalytic subunits of class IA PI3 kinases (PI3K) (1). The p85α protein consists of five domains (Fig. 1): an N-terminal Src homology 3 (SH3)[5] domain, a Breakpoint Cluster Region (BCR) homology Rac/Cdc42-binding domain flanked by two proline-rich motifs (PR1 and PR2), and two Src homology 2 domains (nSH2 and cSH2) that flank the coiled-coil inter-SH2 domain (iSH2). The iSH2 domain binds to the N-terminal adaptor-binding domain of p110α, p110β, and p110δ, yielding a stable low activity heterodimer. Activation of p85/p110 heterodimers by receptor tyrosine kinases requires binding of the nSH2 and cSH2 domains to phosphorylated Y*XX*M motifs in the receptor tyrosine kinases themselves or in adaptors like IRS-1, which relieves inhibitory contacts between the SH2 domains and p110 (2). In cells, activated p85/p110 heterodimers phosphorylate phosphatidylinositol 4,5-bisphosphate to generate phosphatidylinositol 3,4,5-trisphosphate. The lipid phosphatase PTEN antagonizes PI3K signaling by dephosphorylating phosphatidylinositol 3,4,5-trisphosphate (3).

[1] Both authors contributed equally to this work.
[2] To whom correspondence may be addressed: Dept. of Biochemistry, Albert Einstein College of Medicine, 1300 Morris Park Ave., Bronx, NY 10461. Tel.: 718-430-3179; E-mail: michael.brenowitz@einstein.yu.edu.
[3] To whom correspondence may be addressed: Dept. of Biochemistry, Albert Einstein College of Medicine, 1300 Morris Park Ave., Bronx, NY 10461. Tel.: 718-430-2741; E-mail: anne.bresnick@einstein.yu.edu.
[4] To whom correspondence may be addressed: Dept. of Molecular Pharmacology, Albert Einstein College of Medicine, 1300 Morris Park Ave., Bronx, NY 10461. Tel.: 718-430-2153; E-mail: jonathan.backer@einstein.yu.edu.

[5] The abbreviations used are: SH2 and SH3, Src homology 2 and 3, respectively; AUC, analytical ultracentrifugation; BCR, Breakpoint Cluster Region; FFS, fluorescence fluctuation spectroscopy; SAXS, small angle x-ray scattering; SEQ, sedimentation equilibrium; SV, sedimentation velocity; PTEN, phosphatase and tensin homologue deleted on chromosome ten; PR, proline-rich; GTPγS, guanosine 5'-3-*O*-(thio)triphosphate; DSS, disuccinimidyl suberate; DST, disuccinimidyl tartrate; PDB, Protein Data Bank.

Given their modular structure, it is not surprising that p85 subunits participate in intra- and intermolecular interactions in addition to binding p110. p85α/p110 heterodimers are activated by binding of the p85α BCR domain to GTP-bound Rac (4) and Cdc42 (5) as well as the binding of proline-rich domains to SH3 domains from Src family kinases (6). The binding of the influenza protein NS1 similarly activates p85β/p110 heterodimers (7). The iSH2 domains of both p85α and p85β bind the tumor suppressor BRD7, resulting in their nuclear translocation and sequestration from cytosolic p110 (8). Independently of p110, the N terminus of p85α binds PTEN, protecting the latter from degradation and negatively regulating PIP3 production in cells (9–11).

The proline-rich motifs that flank the BCR domain both contain consensus SH3-binding sequences (12). Dimerization of p85α as well as the SH3-PR1-BCR fragment of p85α (residues 1–333; Fig. 1*B*) has been reported, and peptides derived from the PR1 motif disrupt p85α dimerization (13). These results show that intermolecular SH3-PR1 interactions in the native protein are involved in p85α dimerization. *In vivo* dimerization has been demonstrated by reciprocal immunoprecipitation of differentially epitope-tagged p85α in several cell lines (11). A p85α mutation, identified in a human endometrial carcinoma, truncates p85α midway through the BCR domain at residue 160; expression of this mutant is proposed to activate PI3K signaling by inhibiting homodimerization of endogenous p85α, thereby blocking its stabilization of PTEN. The pathological consequence of this mutation highlights the biological importance of the p85α dimer (11).

Because p85α plays a central regulatory role in the PI3K signaling pathway, characterization of its structure and assembly dynamics is crucial to understanding its function in both normal physiology and disease. Our study combines *in vivo* and *in vitro* solution characterization of p85α dimerization with integrative multistate modeling of its global architecture using complementary analytical approaches (14–20). We have characterized the reversible monomer-dimer equilibrium of p85α, showing that dimerization is mediated by multiple domain contacts. Further, we have defined solution conditions under which the protein is monomeric or predominantly dimeric and used these conditions for small angle x-ray scattering (SAXS) and chemical cross-linking studies that have informed the structural modeling of the p85α dimer. Our study provides new insight into p85α dimerization, suggesting that p85α is a highly dynamic molecule whose conformational flexibility allows it to efficiently exchange among multiple binding partners.

Experimental Procedures

Expression and Purification of Cysteine-free p85α

Wild-type human p85α was cloned into the pGEX-6P-1 bacterial expression vector (GE Healthcare) using the BamHI-EcoRI sites. Its six cysteines were mutated (C146S, C167S, C498S, C656S, C659V, and C670L) to generate cysteine-free p85α. Hereafter, we refer to "cysteine-free p85α" as p85α and the wild type protein as "native p85α." Similarly, truncation mutants will be referred to as p85α with superscripts denoting the residues included in the fragment. The construct coding for

p85α was expressed in BL21-CodonPlus competent cells (Agilent Technologies), which were induced overnight with 0.4 mM isopropyl β-D-1-thiogalactopyranoside at 25 °C. The cells were harvested by centrifugation, and the pellets were resuspended on ice in lysis buffer (PBS containing 4 mM DTT, 2 mM EDTA, 2 mM PMSF, 2.5 units/ml Pierce universal nuclease for cell lysis (Thermo Scientific) and Roche cOmplete Mini Protease Inhibitor Tablets (Roche Diagnostics).

The cells were lysed by sonication in an ice bath using a Branson sonicator with a microprobe tip at output level 5 for 30 s followed by 30 s on ice for five cycles. The lysate was brought to 1% Triton X-100, incubated for 20 min at 4 °C on a rotating wheel, and centrifuged at 15,000 rpm in an SS-34 rotor for 20 min at 4 °C. The supernatant was incubated with Pierce glutathione-agarose (Thermo Scientific) for 2–4 h at 4 °C on a rotating wheel. The resin was washed three times by resuspension in 10 column volumes of 50 mM Tris, 150 mM NaCl, pH 8.0. p85α was cleaved from the GST with PreScission protease (GE Healthcare) overnight at 4 °C in cleavage buffer (50 mM Tris, 150 mM NaCl, 1 mM EDTA, 1 mM DTT, pH 8.0) on a rotating wheel. The resin was transferred to a chromatography column, and supernatant containing the cleaved protein was collected, along with two washes of 1 column volume of cleavage buffer each. The PreScission cleavage reaction leaves five residues (GPLGS) at the N terminus preceding the p85α sequence.

The resultant p85α was dialyzed overnight into Mono Q buffer (20 mM Tris, 20 mM NaCl, pH 8.0), loaded onto a Mono Q 10/100 GL anion exchange column (GE Healthcare), and eluted with a 0–350 mM NaCl gradient over 40 column volumes. The peak fractions were analyzed by SDS-PAGE, pooled, concentrated, and loaded onto a HiLoad 26/60 Superdex 200 prep grade gel filtration column (GE Healthcare) equilibrated in gel filtration buffer (50 mM Tris, 300 mM NaCl, pH 8.0). Fractions were analyzed by SDS-PAGE, and those containing >95% pure p85α were pooled and concentrated for use or storage at −80 °C. Stored protein was thawed on ice and centrifuged using a TLA-120.2 rotor (Beckman Coulter) at 80,000 rpm for 15 min at 4 °C prior to use. Protein concentrations were measured using UV absorbance at 280 nm (Nanodrop 2000 UV-visible spectrophotometer, Thermo Scientific) and corresponding extinction coefficients were calculated from protein sequences using ExPASy ProtParam. Protein mass was confirmed via mass spectrometry to be 83,938.6 Da (based on the sequence, the calculated mass is 83,951.6 Da).

Truncated fragments of p85α (Fig. 1) were expressed from the corresponding cDNAs that were synthesized by PCR and ligated into pGEX-6P-1 using the BamHI-EcoRI sites. All constructs were verified by sequencing. The truncated fragments of p85α were expressed and purified using the same protocol described for the full-length protein. For binding assays, native GST-p85α and GST-p85α were purified as described above except that p85α was not cleaved from the glutathione-agarose. SDS-PAGE and Coomassie staining were used to quantitate bead-bound GST fusion proteins. Beads were either stored at 4 °C for up to 1 week or frozen in 50% glycerol at −20 °C.

Assembly of the p85α Homodimer

In Vitro Binding Assays

HEK293T cells were transfected with wild-type N-Myc-p110α using Fugene HD for 48 h. Cells were lysed on ice in lysis buffer (20 mM Tris-HCl (pH 8.1), 137 mM NaCl, 1 mM MgCl₂, 1 mM CaCl₂, 10% (v/v) glycerol, Nonidet P-40; 150 μM vanadate, 1 mM phenylmethylsulfonyl fluoride, cOmplete protein inhibitor cocktail (Roche), and phosphatase inhibitor mixtures (Sigma)), followed by incubation on a rotating wheel for 20 min at 4 °C and centrifugation at 13,000 rpm for 10 min. The clarified supernatant was then incubated with rotation for 2 h at 4 °C with glutathione-Sepharose beads or beads complexed with GST-p85α or native GST-p85α. The beads were washed three times with PBS containing 1% Nonidet P-40 and once with PBS and boiled in 2× Laemmli sample buffer for analysis by SDS-PAGE. Membranes were blotted with an anti-Myc antibody (Cell Signaling Technologies) and developed with ECL Western blotting substrate (Pierce).

For Rac binding, GST-Rac was bacterially produced and bound to glutathione-Sepharose, followed by loading without or with GTPγS (21), and incubated with rotation for 2 h at 4 °C with p85α(1–432). The glutathione-Sepharose beads were washed three times with PBS containing 1% Nonidet P-40 and once with PBS and boiled in 2× Laemmli sample buffer for analysis by SDS-PAGE. Membranes were blotted with in-house anti-p85α-nSH2 antibody and developed with ECL Western blotting substrate (Pierce).

Lipid Kinase Assay

N-Myc-p110α was immunopurified from transiently transfected HEK293T cells as above. Protein-G pellets were washed, incubated without or with bacterially produced GST-p85α or native GST-p85α, and assayed for lipid kinase activity as described previously (22).

SH2-Phosphopeptide Binding

GST-p85α-cSH2 and native GST-p85α-cSH2 constructs (residues 617–724) were expressed in BL-21 *Escherichia coli*, processed as above, and partially purified by elution with 20 mM glutathione from glutathione-Sepharose beads. A tyrosine phosphopeptide containing the photoactivatable amino acid benzoyl phenylalanine (Bpa) (Gly-Asp-Gly-Tyr(P)-Bpa-Pro-Met-Ser-Pro-Lys-Ser) was N-terminally labeled with ^{125}I-Bolton-Hunter reagent and desalted by chromatography on Sephadex G-10. The labeled peptide (4.7 μM final, 3×10^6 cpm/assay) was incubated with 2 μg of GST-cSH2 domain in the absence or presence of 250 μM unlabeled peptide. The samples were irradiated on ice with a 200-nm UV lamp at a distance of 1 cm for 1 h, boiled in Laemmli sample buffer, and analyzed by SDS-PAGE and autoradiography.

Analytical Ultracentrifugation (AUC)

AUC studies were conducted with a Beckman Optima XL-I centrifuge using the AN-60Ti rotor. The absorption optics were set to 280 nm. Protein samples were run in either the low or high salt SAXS buffers described below at temperatures ranging from 4 to 37 °C. An SH3-binding peptide (RPLP-PRPGA) used to inhibit dimerization was synthesized by Gen-

Script and kept at −20 °C as a concentrated stock solution that was thawed and diluted into the buffer appropriate for each experiment. Sednterp (available online from the University of New Hampshire) was used to calculate the partial specific volume of the proteins from their sequence and the density and viscosity of the buffers. The sedimentation parameters were corrected to standard conditions (20,w) using these values.

For sedimentation velocity (SV) experiments, 300 μl of sample and an equal volume of buffer were loaded into two-sector cell assemblies. Three concentrations of each protein corresponding to A_{280} ~0.1, 0.4, and 1.0 (equivalent to 1.2, 3.6, and 9.6 μM p85α monomer) were analyzed for each solution condition. 60–70 scans were collected over the course of a sedimentation velocity run. A subset of scans, beginning with those where a clear plateau was evident between the meniscus and the boundary, were selected for time-derivative analysis using DCDT+ version 2.4.2 (23, 24). The SV experiments presented in this paper were conducted at 42,000 rpm. For sedimentation equilibrium (SEQ) experiments, 120 μl each of sample and buffer were loaded into six-channel cell assemblies at the concentrations noted above. Data were taken following initial equilibration for 24 h at the indicated speed and then following a second 24-h equilibration at higher speed. Scans were also taken after 22 h so that equilibration could be confirmed. The p85α EQ experiments were equilibrated at 8,000 and then 16,000 rpm; p85α(1–600) was equilibrated at 9,000 and then 16,000 rpm; p85α(1–432) was equilibrated at 10,000 and then 20,000 rpm; p85α(1–333) was equilibrated at 18,000 and then 25,000 rpm; and p85α(78–322) was equilibrated at 20,000 and then 30,000 rpm. The equilibrium experiments were globally analyzed using HeteroAnalysis version 1.1.58 (25, 26).

Fluorescence Fluctuation Spectroscopy (FFS)

p85α and native p85α were cloned into pEGFP-N1 using the EcoRI-BamHI sites. Native p85α was also used as a template for site-directed mutagenesis of proline residues 96 and 99 to alanine and methionine 176 to alanine (PR1/M176A). FFS experiments were performed on a home-built two-photon fluorescence fluctuation microscope described previously (27), which is composed of an Olympus IX-71 and a mode-locked Ti:Sapphire laser (Chameleon Ultra, Coherent). A ×60 Plan-Apo oil immersion objective (numerical aperture = 1.4; Olympus) was used to focus the laser and collect the fluorescence. Two short pass filters (ET680sp-2p8, Chroma) eliminated scattered laser light. A band pass emission filter further filtered the fluorescence (FF01-525/50-01, Semrock). An avalanche photo-diode detector (SPCM-AQR-14, PerkinElmer Life Sciences) was directly connected to a data acquisition card (FLEX02, Correlator.com). The recorded photon counts were stored and later analyzed with programs written in IDL (ITT Exelis). The normalized brightness b (28) is defined as $b = \lambda_{app}/\lambda_{EGFP}$, which measures the oligomerization of the target protein. The sample apparent brightness λ_{app} is measured by generalized Mandel's Q parameter analysis (29). The brightness λ_{EGFP} is obtained in calibration experiments by measuring cells transfected with EGFP.

Chemical Cross-linking Analysis of p85α and p85α(1–333)

p85α and p85α(1–333) (Fig. 1*B*) were dialyzed into 20 mM HEPES, pH 8.0, containing 20 mM NaCl, a solution condition that favors p85α dimerization (Fig. 3*A*). 12 μM p85α was incubated with 0.5 mM disuccinimidyl suberate (DSS) for 15 min on ice with gentle agitation. 30 μm p85α(1–333) was incubated with a 50-fold molar excess of disuccinimidyl tartrate (DST) freshly prepared in 100% DMSO for 15 min at room temperature with gentle agitation. The DSS and DST cross-linking reactions were quenched with the addition of Tris to a final concentration of 100 mM. Dimer formation was assessed using SDS-PAGE followed by Coomassie staining.

After electrophoresis, the gel region corresponding to p85α or p85α(1–333) dimer was excised and digested in-gel with trypsin to release the cross-linked peptides. The samples were processed and analyzed by mass spectrometry as described previously (30, 31, 86). Briefly, the cross-linked target proteins were in-gel digested with trypsin. After proteolysis, cross-linked peptides were extracted, dried in a SpeedVac (Savant), and desalted/purified on a C18 solid phase extraction column (Waters). Next, the cross-linked peptides were enriched by size exclusion chromatography and analyzed by an Orbitrap Q Exactive (QE) Plus mass spectrometer (Thermo Fisher Scientific). The QE Plus instrument was directly coupled to an EasyLC system (Thermo Fisher Scientific). The cross-linked peptides were loaded onto an Easy-Spray column heated at 35 °C (C18, 3-μm particle size, 200-Å pore size, and 50 μm × 15 cm; Thermo Fisher Scientific) and eluted using a 120-min LC gradient (2–10% B, 0–6 min; 10–35% B, 6–102 min; 35–100% B, 102–113 min; followed by equilibration, where mobile phase A consisted of 0.1% formic acid and mobile phase B consisted of 0.1% formic acid in acetonitrile) at a flow rate of ~300 nl/min. The spray voltage was 2.0 kV, and the 10 most abundant ions (with a charge stage of 4–7) were selected and fragmented by higher energy collisional dissociation (normalized higher energy collisional dissociation energy 28).

The raw data were transformed to MGF (mascot generic format) and searched by pLink (32). An initial MS1 search window of 5 Da was allowed to cover all isotopic peaks of the cross-linked peptides. The data were automatically filtered using a mass accuracy of MS1 $\leq$ 10 ppm and MS2 $\leq$ 20 ppm of the theoretical monoisotopic (A0) and other isotopic masses (A+1, A+2, A+3, and A+4) as specified in the software. An additional search parameter was methionine oxidation as a variable modification. A maximum of two trypsin missed cleavage sites was allowed. The initial search results were obtained using a default 5% false discovery rate, as predicted by a target decoy search strategy. In our analysis, we treated the 5% false discovery rate as a rough initial filter of the raw data. We then manually inspected all of the cross-link MS/MS spectra that were assigned by the software and applied additional filters to remove potential false positive identifications from the data set (30, 31). This processing resulted in the removal of ~30% of the cross-linking data from the 5% false discovery rate results, ensuring high quality data for structural modeling.

Small Angle X-ray Scattering (SAXS)

SAXS profiles of full-length and truncated p85α were measured at concentrations ranging from 0.5 to 5.0 mg/ml in either 20 mM NaCl, 20 mM HEPES, 5% glycerol, pH 8.0, or 500 mM NaCl, 20 mM HEPES, 5% glycerol, pH 7.5, at temperatures of 10 and 25 °C. The glycerol protects the proteins from radiation damage during x-ray exposure (33). All solutions were filtered through 0.1-μm membranes (Millipore).

SAXS measurements were carried out at Beamline 4-2 of the Stanford Synchrotron Radiation Lightsource (SSRL) in the SLAC National Accelerator Laboratory. At SSRL, the beam energy and current were 11 keV and 500 mA, respectively. A silver behenate sample was used to calibrate the *q*-range and detector distance. Data collection was controlled with Blu-Ice (34). We used an automatic sample delivery system equipped with a 1.5-mm diameter thin wall quartz capillary, within which a sample aliquot was oscillated in the x-ray beam to minimize radiation damage (35). The sample was placed at 1.7 meters from an MX225-HE (Rayonix) CCD detector with a binned pixel size of 293 × 293 μm.

Up to 24 1-s exposures were used for each sample, and buffers were maintained at 10–25 °C. The SAXS profile of each buffer was obtained under the same conditions and subtracted from the protein SAXS profile. Each of the resulting diffraction images was scaled using the transmitted beam intensity, azimuthally integrated by SASTool (SASTool 2013, SLAC National Accelerator Laboratory), and averaged to obtain fully processed data in the form of intensity *versus q* ($q = 4\pi\sin(\theta)/\lambda$, where θ represents one-half of the scattering angle, and λ is x-ray wavelength).

The buffer-subtracted SAXS profiles were initially analyzed using the ATSAS package (37) to calculate radius of gyration (R_g), maximum particle size (D_{max}), pair distribution function ($P(r)$), and Porod volume (Table 1). The molecular weight (MW_{SAXS}) of each SAXS sample was estimated using SAXS MOW (38) with a threshold of $Q_{max} = 0.2$–0.3 Å^{-1}.

The *ab initio* shapes of the p85α(1–333) and p85α dimers (Figs. 6*A* and 7*A*, respectively; *gray envelope*) were generated from the corresponding dimer SAXS profile by running DAMMIF (39) 20 times and then refined through an additional 50 DAMMIN (40) runs followed by superposition and averaging with DAMAVER (41).

Integrative Multistate Modeling of p85α and p85α(1–333) Dimers

We computed ensembles of atomic multistate models of the p85α(1–333) dimer and the p85α dimer based on SAXS profiles, chemical cross-links, the assembly state determined by AUC, and crystal structures of its domains and homologs. A "multistate model" is a model that specifies multiple discrete structural states of the system, all of which are required to explain the input information (19, 42–44). In contrast, in an ensemble of models, any single model explains the input information. This approach proceeds through four stages: 1) data gathering, 2) representation of subunits and translation of the data into spatial restraints, 3) conformational sampling to produce the most parsimonious multistate model consistent with

all available data and information, and 4) analysis and assessment of the multistate model. Our protocol was scripted using the Python Modeling Interface (PMI), version 2f82087, a library for modeling macromolecular complexes based on our open source Integrative Modeling Platform package release 2.5 (14–20). Files for the input data, modeling scripts, output model structures in multiple states, and additional figures and tables are available on the Sali Lab p85 webpage. The procedure for each stage is summarized below.

Stage 1: Data Gathering—SAXS profiles, assembly states, 231 DSS chemical cross-links for p85α, and 25 DST chemical cross-links for p85α(1–333) were obtained as described above. HHpred (45, 46) and ModWeb (47) identified the atomic structures of *Homo sapiens* p85α(2–82) (PDB code 3I5R (48), chain A), p85α(115–298) (PDB code 1PBW (49), chain A), p85α(324–433) (PDB code 2IUG (50), chain A), p85α(326–579) (PDB codes 3HIZ and 3HHM (51), chain B), p85α(431–600) (PDB code 2V1Y (52), chain B), p85α(617–721) (PDB code 1H9O (53), chain A), and homologs (PDB codes 1PRL (54), chain C, and 2Y3A (55), chain B). DomPRED (56), PSIPRED (57, 58), and DISOPRED (59) predicted domain boundaries, secondary structure segments, and disordered regions, respectively. The intermolecular interaction between SH3 and PR1 domains was confirmed by its disruption by the SH3-binding peptide (RPLPPRPGA).

Stage 2: Subunit Representation and Translation of the Data into Spatial Restraints—The size and shape information contained in SAXS profiles can be used to improve the accuracy of atomic comparative models. An initial atomic model of the p85α dimer was built based on template structures (Stage 1) and SAXS profiles as follows. First, we built 100 atomic comparative models for p85α "monomer" in complex with the SH3-binding PR1-like peptide (RPLPPRPGA) (data not shown), using MODELLER version 9.14 (60) based on the crystal structures and the closest template structures.

The theoretical SAXS profile and the χ value of the fit to the experimental monomer SAXS profile were calculated for each of the 100 comparative models, using FoXS (61, 62). Then these 100 models were ranked by the χ value of the fit. Second, the best scoring monomer model (with a lowest χ value; data not shown) was used as a template for building an initial model of the p85α dimer. We added another copy of the p85α monomer at a random starting position for each sampling run, which resulted in an initial model of the p85α dimer. The SH3-binding PR1-like peptides were removed in the dimer model of p85α to reflect the composition of the SAXS sample.

Next, a monomer model of p85α(1–333) was obtained by removing residues of 334–724 in the best scoring p85α monomer model (data not shown). Similarly, we added another copy of the p85α(1–333) monomer at a random starting position for each sampling run, which resulted in an initial model of the p85α(1–333) dimer. The SH3-binding PR1-like peptides were removed in the dimer model p85α(1–333) to reflect the composition of the SAXS sample.

Domains were coarse-grained using beads representing individual residues and arranged into either a rigid body or a flexible string based on the available crystallographic structures or comparative models (30). The coordinates of a bead were those

of the corresponding C_α atoms. In a rigid body, the beads have their relative distances constrained during conformational sampling in Stage 3, whereas in a flexible string, the beads are restrained by the sequence connectivity, as described below. The residues in the rigid bodies and flexible strings corresponded to 87 and 13% of p85α, respectively.

With this representation, the information gathered in Stage 1 was converted into spatial restraints and constraints. We used different subsets of the spatial restraints and constraints (*i.e.* restraint subsets) for different sampling runs to maximize sampling efficiency. 231 DSS chemical cross-links for the p85α dimer and 25 DST chemical cross-links for the p85α(1–333) dimer were used to construct a Bayesian scoring function that restrained the distances spanned by the cross-linked residues (64). The cross-link restraints were applied to the corresponding bead pairs, taking into account the difficulty of distinguishing intermolecular *versus* intramolecular cross-links in two identical p85α subunits in the dimer; an ambiguous cross-link restraint considers all possible pairwise assignments. For example, a restraint between residues 438 and 519 is evaluated (64) from the following distances: "438@p85α.*1* to 519@p85α.*1*"; "438@p85α.*1* to 519@p85α.*2*"; "438@p85α.*2* to 519@p85α.*1*"; and "438@p85α.*2* to 519@p85α.*2*" followed by scoring only the least violated distance.

Four homodimer cross-links between residues 438–438, 480–480, 530–530, and 567–567 were transformed to upper harmonic distance restraints (up to 20 Å), enforcing the parallel intermolecular orientation of two iSH2 domains. In contrast, four chemical cross-links of 438–519, 438–530, 447–519, and 447–530 were transformed to upper harmonic distance restraints (up to 20 Å), enforcing the anti-parallel intermolecular orientation of two iSH2 domains. In addition, a homodimer cross-link of 633–633 was transformed to upper harmonic distance restraints (up to 20 Å), enforcing the intermolecular interaction of two cSH2 domains.

Notably, we applied five upper harmonic distance restraints on residues 14–92, 51–92, 54–92, 70–92, and 73–92 (up to 13.5 Å) to retain the intermolecular interaction sites between SH3 and PR1 domains, each one residing in a different subunit of the dimer. A crystal structure of the SH3 domain bound to a polyproline peptide (PDB code 1PRL) was used as a template for interaction site identification (54). Initially, both single and double intermolecular SH3-PR1 interactions were evaluated through the multistate search for the p85α(1–333) dimer, leading to a conclusion that the double intermolecular SH3-PR1 interactions are dominant in the p85α dimer. Thus, we confined double intermolecular SH3-PR1 interactions in all restraint subsets of the p85α dimer.

The excluded volume restraints were applied to each bead, using the statistical relationship between the volume and the residue that it covered (15, 30, 65). We applied the sequence connectivity restraint, using a harmonic upper bound function of the distance between consecutive beads in a subunit, with a threshold distance equal to 4 times the sum of the radii of the two connected beads. The bead radius was calculated from the excluded volume of the corresponding bead, assuming standard protein density (15, 30, 65, 66). Last, the most populated state of the p85α(1–333) dimer (40.3% population) was further

constrained during conformational sampling of the p85α dimer in selected restraint subsets.

Stage 3: Conformational Sampling to Produce the Most Parsimonious Multistate Model Consistent with All Available Data and Information—The initial dimer models of p85α and p85α(1–333) were subjected to conformational sampling using replica exchange Gibbs sampling, based on the Metropolis Monte Carlo algorithm (30, 67). The Monte Carlo moves included random translation and rotation of rigid bodies (up to 0.5 Å and 0.02 radians, respectively) and random translation of individual beads in the flexible segments up to 0.5 Å. For each of the restraint subsets, 2–3 independent sampling calculations were performed, each one starting with a random initial configuration. 4–16 replicas were used with temperatures ranging between 1.0 and 2.5. A model was saved every 10 Gibbs sampling steps, each consisting of a cycle of Monte Carlo steps that moved every rigid body and flexible bead once (30). The sampling produced ~80,000 (from eight independent runs of the p85α(1–333) dimer) and ~200,000 models (from 45 independent runs of the p85α dimer) that were submitted for subsequent multistate analysis. The entire sampling procedure took 1 week on a cluster of ~400 computational cores.

The resulting ~80,000 and ~200,000 models obtained for the p85α(1–333) and p85α dimers, respectively, were pruned to identify multistate models that satisfied both the experimental SAXS profiles and the chemical cross-link data sets. MultiFoXS (42, 69) was used to prune the data sets with a composite score defined as a sum of the "multistate SAXS score" (70) and the "multistate cross-link score."

The multistate SAXS score (70) is the χ value for the comparison of the "multistate SAXS profile" with the experimental profile; the multistate SAXS profile is a weighted average of the theoretical SAXS profiles for the selected subset of states, each one calculated using FoXS (61, 62). The side chains of whole residues in each state were reconstructed using PULCHRA version 3.06 (71) for higher accuracy in the theoretical SAXS profiles.

The multistate cross-link score is a negative value of the proportion of chemical cross-links satisfied in the selected subset of states; a cross-link restraint was considered to be satisfied by the subset if the minimum C_α–C_α distance of the corresponding residue pairs was smaller than a distance threshold of 35 Å, considering restraint ambiguity (above).

Independent fitting of subsets ranging from 1 to 9 states showed that five states of each protein were sufficient to account for both the experimental SAXS profiles and the chemical cross-link data sets.

Stage 4: Analysis and Assessment of the Multistate Model—The most populated state in the multistate model was used as a reference for rigid body least-squares superposition of the remaining states. The multistate models of p85α(1–333) and p85α dimers were visualized with UCSF Chimera (Figs. 6C and 7C, respectively) (72). The template modeling scores for each pair of the individual states were calculated using the corresponding Web server (73).

The multistate model was assessed for how well it satisfied the data from which it was computed, including chemical cross-links, excluded volume, sequence connectivity, and SAXS profiles. We validated the multistate model against each of the chemical cross-links; a cross-link restraint was considered to be satisfied by the multistate model if the minimum C_α–C_α distance of the corresponding residue pairs was <35 Å. The excluded volume and sequence connectivity restraints were considered to be satisfied by an individual state if their combined score was <100. Finally, The χ value and the residual plot were used for the comparison of the multistate SAXS profile with the experimental profile.

Results

Characterization of Cysteine-free p85α—Purification of p85α from bacterial expression systems is hampered by poor protein stability.[6] We noted substantial improvements in protein purity and yield while preparing a cysteine-free mutant of p85α for use in site-specific spin labeling studies (74). Therefore, we mutated each of the six cysteines in p85α (two in the BCR domain, one in the iSH2 domain, and three in the cSH2 domain) to serine, leucine, or valine (Fig. 1A), depending on whether the cysteines were predicted to participate in hydrophobic interactions based on crystal structures of isolated domains. As stated under "Experimental Procedures," the resultant protein is herein referred to as "p85α" and the wild type protein as "native p85α." p85α robustly expresses and is readily purified in milligram quantities (10–15 mg/liter of bacterial culture). Similar protein yield and stability were achieved with the p85α fragments that were studied (Fig. 1B). Creation of cysteine-free p85α enabled the solution assembly and structural studies described in this paper.

We performed several assays to demonstrate the functional integrity of each cysteine-containing domain of p85α relative to the native protein. Using immunoprecipitation and kinase assays, we found that the two proteins showed similar binding to p110α and inhibition of its kinase activity (Fig. 2, A and B). The cSH2 domains of both p85α proteins were comparably labeled by a photoactivatable ^{125}I-YXXM phosphopeptide; labeling was almost completely eliminated by competition with unlabeled peptide, showing that the reaction is specific (Fig. 2C). Last, the interaction of the small GTPase Rac1 with the p85α(1–432) (4) showed the expected GTP dependence, demonstrating that the BCR domain was unaffected by mutation of its cysteine residues (Fig. 2D). Taken together, these results show that substitution of the cysteine residues in p85α has no appreciable effect on its biochemical activity.

p85α Dimerization in Vitro—The ability of p85α to self-assemble *in vitro* has been documented (13). A question that motivated our analysis of p85α dimerization is whether it can play a role in the assembly of the various heterologous complexes that regulate PI3K signaling. A second motivation was to enable structure and assembly studies by identifying solution conditions under which p85α is predominantly monomeric or dimeric. We utilized two modes of AUC analysis to characterize p85α self-assembly. SV analysis measures the sedimentation rate and yields two coefficients, sedimentation (*S*) and diffusion (*D*), whose ratio *S/D* can provide the molecular weight. However, because *S* and *D* are dependent on both molecular size and

---
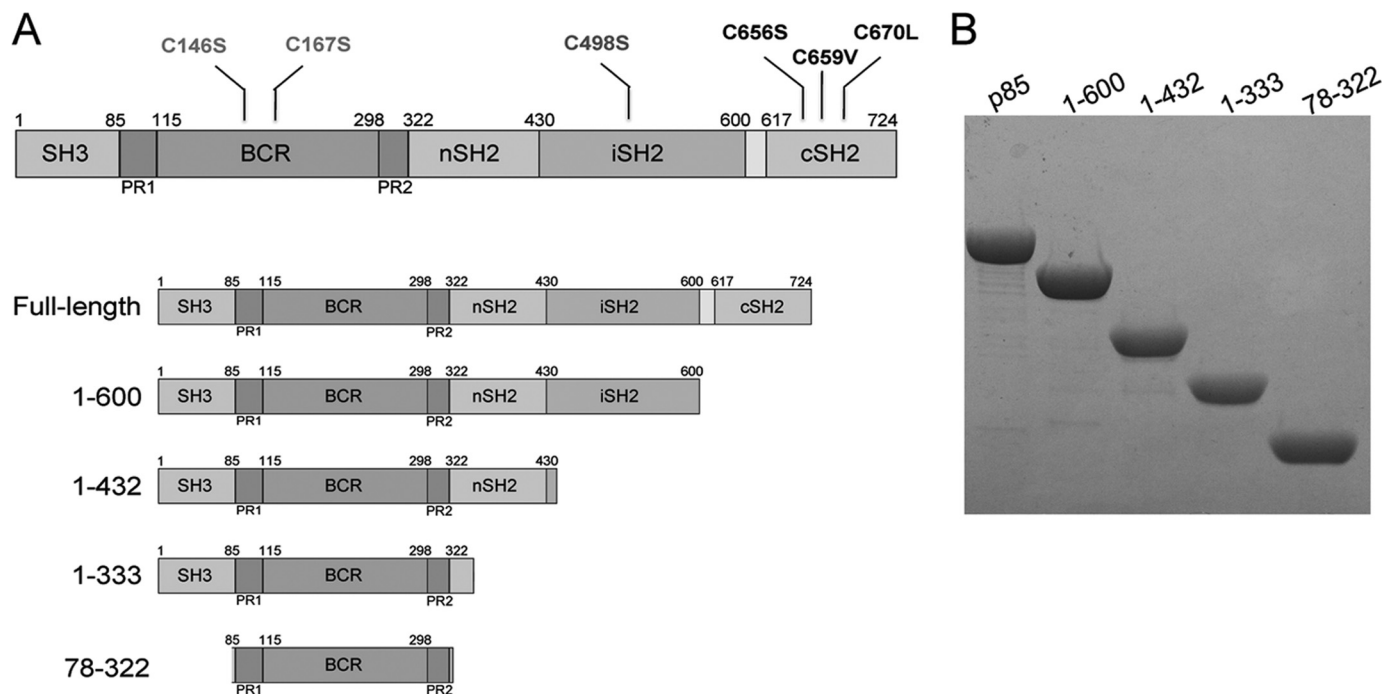
[6] H. Wu and J. M. Backer, unpublished data.

FIGURE 1. **Cysteine-free p85α and fragments.** *A*, the six cysteines of wild-type human p85α were mutated (C146S, C167S, C498S, C656S, C659V, and C670L) to generate cysteine-free recombinant p85α, herein referred to as p85α. Four 85α truncations were also prepared. *B*, Coomassie-stained SDS-polyacrylamide gel of purified p85α and fragments.

shape, their ratio can yield erroneous molecular weights. Erroneous molecular weight values calculated from S/D can also result from protein self-association. Therefore, we also conducted SEQ analyses, whose results are not dependent on molecular shape, to determine the molecular weight, stoichiometry, and dissociation constant (K_d) of p85α and its fragments.

SV experiments with p85α analyzed by the time-derivative method revealed single peaks (Fig. 3*A*), whose $s_{20,w}$ values increased with increasing protein concentration and decreased with increasing temperature and salt concentration (Fig. 3*B*). These observations reveal that p85α undergoes rapidly reversible self-association at micromolar protein concentrations and that the assembly interaction is exothermic with an electrostatic component. The molecular weight values calculated from S/D from these experiments (Fig. 3*A*) proved to be erroneous upon comparison with the SEQ analyses described below (data not shown).

SEQ analysis of p85α was conducted as a function of temperature at both low and high salt conditions at initial protein concentrations ranging from 1.2 to 9.6 μM (Fig. 3, *C* and *D*). The data are consistently described as a monomer-dimer equilibrium (Figs. 3*E* and 4). Adding higher order species does not improve the fit of the assembly models to the data (analysis not shown). The temperature dependence of dimerization is exothermic, as observed by SV; the linear van't Hoff plots reveal different enthalpies at low and high salt ($\Delta H^0 = -23.7$ and -14.3 kcal, respectively; Fig. 3*C*). The salt concentration substantially affects p85α dimerization.

For example, at 10 °C, the values of K_d measured at 20 and 500 mM NaCl differ by almost 40-fold (Fig. 3*F*). p85α remains a mixture of monomer and dimer at 500 mM NaCl with the equi-

librium biased toward monomer at the higher salt. Under conditions of low temperature and low salt, p85α is almost completely dimeric. Conversely, p85α is predominantly monomeric at high temperature and high salt. Studies conducted at approximate physiological salt concentration (140 mM NaCl) are also well described by the monomer-dimer equilibrium with a K_d value comparable with that measured at the high salt concentration (data not shown).

To evaluate the contribution of intermolecular SH3-PR1 interactions to dimerization, we examined dimer formation in the presence a 9-amino acid SH3-binding peptide containing a proline-rich consensus sequence (RPLPPRPGA) that binds the p85α SH3 domain (75). A 25-fold molar excess of peptide (250 μM peptide *versus* 9.6 μM protein) drives the equilibrium completely to monomer regardless of the temperature or salt concentration (data not shown). This reaction occurs presumably by competition of the peptide with the PR1 domains for intermolecular SH3 domain binding. Thus, peptide-bound p85α is an alternative condition for the analysis of monomeric protein.

The results presented above suggest that the intermolecular SH3-PR1 interaction dominates p85α dimerization. To explore possible contributions of other domains to dimerization, we analyzed the assembly of a series of p85α truncations (depicted in Fig. 1*A*). SEQ analysis of the p85α fragment containing only SH3-PR1-BCR-PR2 (p85α(1–333)) reveals 10-fold weaker dimerization compared with the full-length protein (Fig. 3*F*; $K_d = 30.0$ *versus* 2.5 μM at 20 mM NaCl and 10 °C), loss of salt dependence, and diminished enthalpy ($\Delta H^0 = -6.7$ and -11.6 kcal, respectively; Fig. 3*D*). Analysis of a series of more refined truncations shows that it is the cSH2 domain that contributes to p85α dimerization and is the source of the reaction's salt dependence (Fig. 3, *E* and *F*, compare p85α with p85α(1–600)).
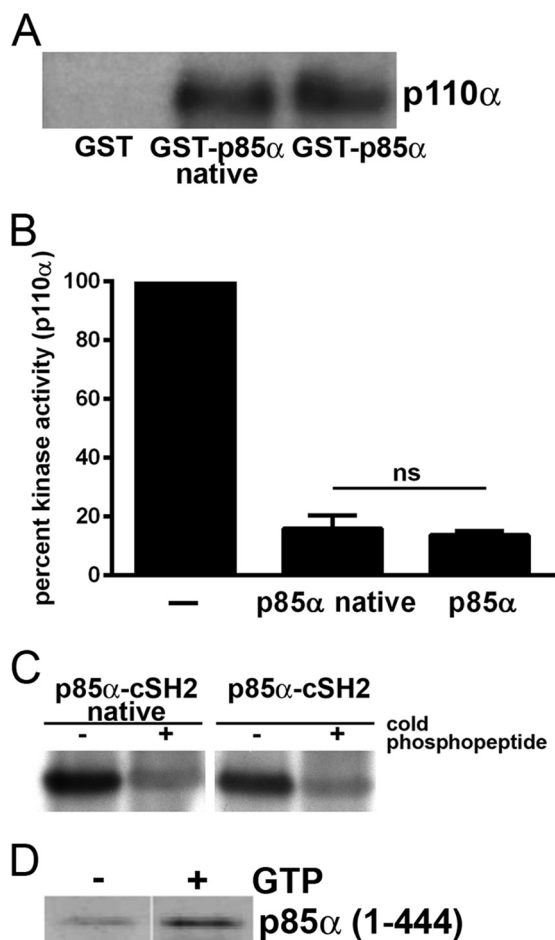
FIGURE 2. **Characterization of cysteine-free p85α.** *A*, immunoblot analysis of Myc-p110α binding to GST alone, GST-p85α, or native GST-p85α. *B*, kinase activity of p110α purified from HEK293T cells in the presence of GST-p85α or native GST-p85α. Shown are the average ± S.E. (*error bars*) from three independent experiments. *ns*, not significant. *C*, binding of GST-cSH2 domains from p85α or native p85α to a photoactivatable ^{125}I-labeled tyrosine phosphopeptide in the absence or presence of unlabeled phosphopeptide. *D*, immunoblot analysis of GST-p85α(1–432) binding to recombinant Rac1 loaded without or with GTPγS.

These data show that cSH2 also contributes to p85α dimerization.

Published studies suggest that the BCR domain is potentially part of the dimer interface (13, 49). To test whether the BCR domain itself dimerizes, we expressed and purified a fragment of p85α corresponding to residues 78–322, which contains the BCR domain flanked by the two proline-rich motifs. SEQ analysis shows that p85α(78–322) does not dimerize; an identical result was obtained for native p85α(78–322), regardless of salt concentration or temperature for either construct (data not shown). These data show that the BCR domain alone does not dimerize.

p85α Dimerization in Vivo—FFS was used to measure dynamic changes in protein association *in vivo*. U2OS cells were transfected with native GFP-p85α, GFP-p85α, or a monomeric GFP control. The brightness of the GFP fluorescence correlates linearly and positively with increasing concentrations of the GFP-p85α fusion protein. In contrast, the brightness of the monomeric GFP control is invariant with concentration. The slopes of the correlations for native p85α and p85α

are identical and appreciably greater than that for GFP alone control (Fig. 5*A*). These data demonstrate that both native p85α and p85α dimerize *in vivo* in a concentration-dependent fashion.

To test the contribution of the SH3-PR1-BCR domains to p85α dimerization *in vivo*, we compared the FFS brightness distributions of native GFP-p85α with those of a mutant p85α in which two key proline residues in PR1 and a methionine residue in the BCR domain were mutated to alanine (p85α$^{PR1/M176A}$). These residues were selected based on studies showing that these mutants inhibit co-immunoprecipitation of tagged p85α constructs in intact cells.[7] The slope of brightness *versus* protein concentration was more than 2-fold greater in U2OS cells transfected with native GFP-p85α as compared with native GFP-p85α$^{PR1/M176A}$, consistent with the mutant exhibiting reduced dimerization *in vivo* (Fig. 5*B*). Because mutation of PR1 and the BCR domain did not completely abolish dimerization, these data indicate that additional domains contribute to p85α dimerization, an observation consistent with our *in vitro* analyses.

SAXS—SAXS is a measure of p85α assembly orthogonal to AUC that provides information about protein size and shape (76). SAXS profiles of p85α and its fragments (Fig. 1) were measured under conditions shown by AUC analysis to favor monomer or dimer. At low salt, we observed by SAXS predominantly p85α dimer at protein concentrations of 12 μM (1.0 mg/ml) at 10 °C (see Fig. 7*B* and Table 1) and 18 μM (1.5 mg/ml) at 25 °C. At the highest protein concentration analyzed (5.0 mg/ml or ~60 μM, greater than that analyzed by AUC), oligomers of higher order than dimer were observed. Saturating concentrations of the SH3-binding peptide drove the equilibrium completely to monomer as measured by AUC.

Our SAXS analysis of p85α(1–333) (SH3-PR1-BCR-PR2) is likewise consistent with the AUC results. At high protein concentrations, the protein is fully dimeric at low salt and low temperature (Fig. 6*B* and Table 1) and salt-independent. In contrast, p85α(78–322) (PR1-BCR-PR2) does not dimerize under any condition, confirming that the intermolecular SH3-PR1 interaction is critical for dimerization. SAXS analysis of p85α(1–432) and p85α(1–600) is consistent with AUC data showing that the salt dependence of dimerization resides within the cSH2 domain (residues 617–724). The analysis also suggests that the iSH2 domain (residues 430–600) makes a small (2-fold) contribution to p85α dimerization.

Chemical Cross-linking of p85α and p85α(1–333) Dimers—Chemical cross-linking of p85α(1–333) and p85α dimers with DST and DSS, respectively, was carried out under solution conditions favorable to dimer formation. The chemical cross-linking reactions were optimized for mass spectrometric analysis. The covalent adducts were analyzed by mass spectrometry. Our cross-linking and mass spectrometric analysis revealed 25 and 231 unique cross-linked residue pairs, respectively, for the p85α(1–333) and p85α dimers (Figs. 6*D* and 7*D*). The overall connectivity pattern of the DST cross-links for p85α(1–333) is similar to that of the DSS cross-links for the same portions of

---

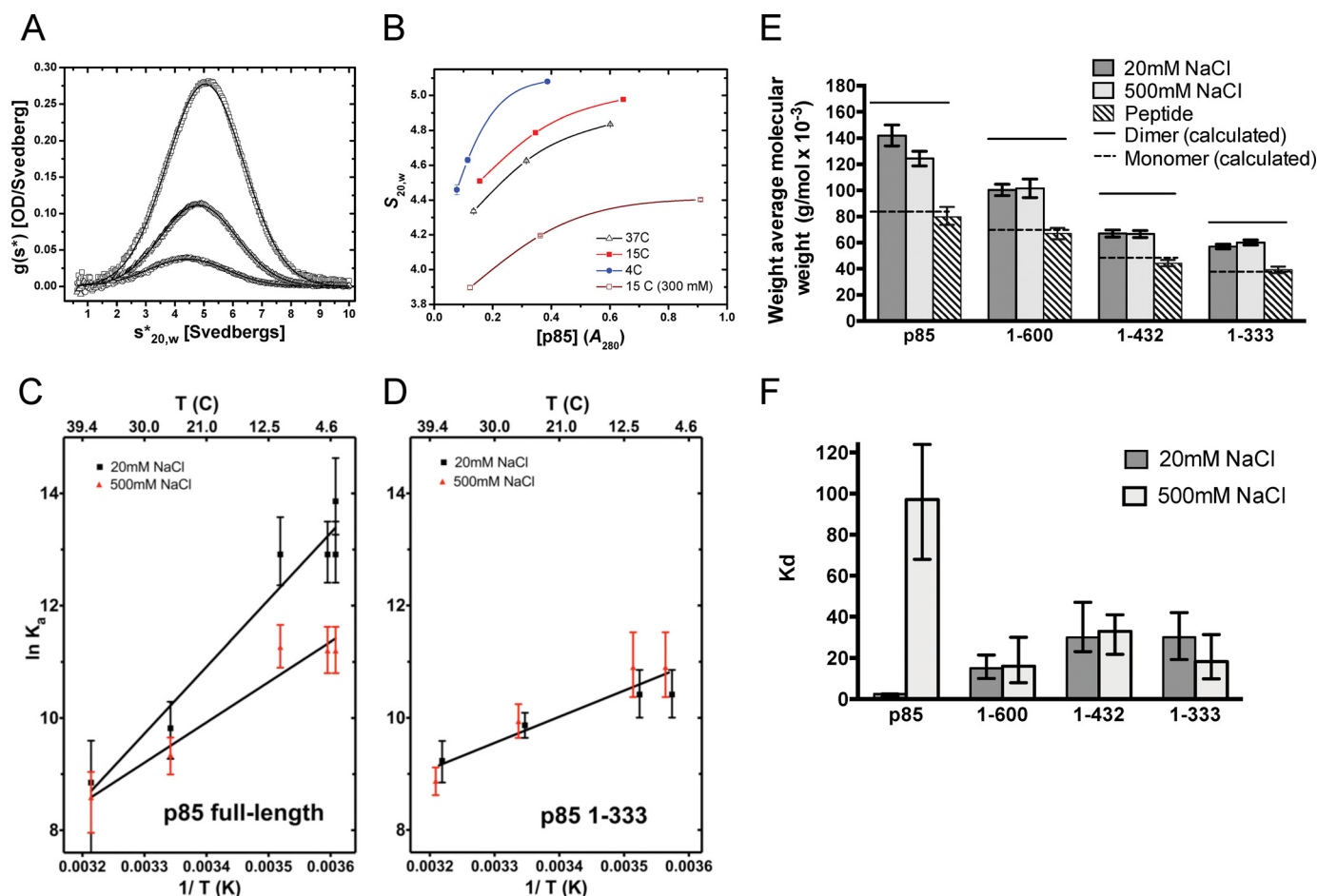[7] G. B. Mills, personal communication.

FIGURE 3. **p85α dimerization *in vitro* measured by AUC.** *A*, sedimentation coefficient distribution, $g(s^*)$, obtained from sedimentation velocity analysis of p85α at three concentrations (1.2, 3.6, and 9.5 μM) in 20 mM NaCl-containing buffer at 4 °C. All sedimentation coefficient (S, in Svedberg units) values presented in the paper have been corrected to 20 °C and the density of water ($s_{20,w}$) to allow comparison of data from experiments performed in different buffers and temperatures. *B*, plot of sedimentation velocity data showing S as a function of p85α concentration (absorbance at 280 nm) at 4, 15, 37, and 15 °C in 300 mM NaCl-containing buffer. *C* and *D*, van't Hoff plots relating the association constant (K_a) determined by sedimentation equilibrium analysis as a function of temperature for full-length p85α (*C*) and p85α(1–333) (*D*) in 20 and 500 mM NaCl-containing buffer. *E*, weight average molecular weights obtained from sedimentation equilibrium analysis of p85α and corresponding fragments in buffer containing either 20 mM NaCl or 500 mM NaCl and at 500 mM NaCl in the presence of 250 μM SH3-binding peptide. *Solid* and *dashed lines*, dimer and monomer molecular weights calculated from sequence, respectively. *F*, dissociation constant (K_d) values for each p85α construct in low and high salt, derived from fitting sedimentation equilibrium data to a monomer-dimer association model. Values are represented with joint confidence intervals of one S.D.

full-length p85α, showing that they provide complementary information on similar conformers. This result demonstrates that the absence of the C-terminal domains does not affect the conformational states sampled by SH3-PR1-BCR-PR2 and supports the use of the p85α(1–333) structural model in modeling the full-length protein as is presented below.

In full-length p85α, cross-links were identified that are consistent with both parallel and antiparallel orientations of the two coiled-coil (iSH2) domains in the dimer. Homodimer cross-links between residues 438–438, 480–480, 530–530, and 567–567 are consistent with the parallel intermolecular orientation, according to the crystal structures (PDB codes 3HIZ and 3HHM (49)) of an isolated iSH2 domain. In contrast, cross-links between residues 438–519, 438–530, 447–519, and 447–530 are compatible with the anti-parallel orientation. These results suggest that the iSH2 domains in p85α can dock in either orientation upon dimerization. Furthermore, many lysine residues formed multiple cross-links spanning over the N- and C-terminal domains (*e.g.* Lys-81, Lys-142, Lys-187, and

Lys-256; Figs. 6*D* and 7*D*), which is also consistent with the p85α dimer being highly dynamic in solution.

We also identified chemical cross-links between residues 633–633 in the cSH2 domains. Although it is impossible to distinguish intermolecular from intramolecular cross-links between non-identical residues in two identical p85α subunits based on the cross-linking data alone, cross-links between identical residues can only be intermolecular. Moreover, the 633–633 cross-link is also consistent with the AUC observation that the cSH2 domain contributes to dimerization.

Integrative Structure Determination of p85α and p85α(1–333) Dimers in Multiple States—We carried out conformational sampling using replica exchange Gibbs sampling based on the Metropolis Monte Carlo algorithm to study the structure and dynamics of p85α dimers in solution (30, 67). We began with the p85α(1–333) dimer (Fig. 1*A*) and tested whether or not the resulting ~80,000 models were consistent with the experimental SAXS profile and the 25 chemical cross-links. Both the SAXS profile and the cross-linking data set were not simultaneously explained by
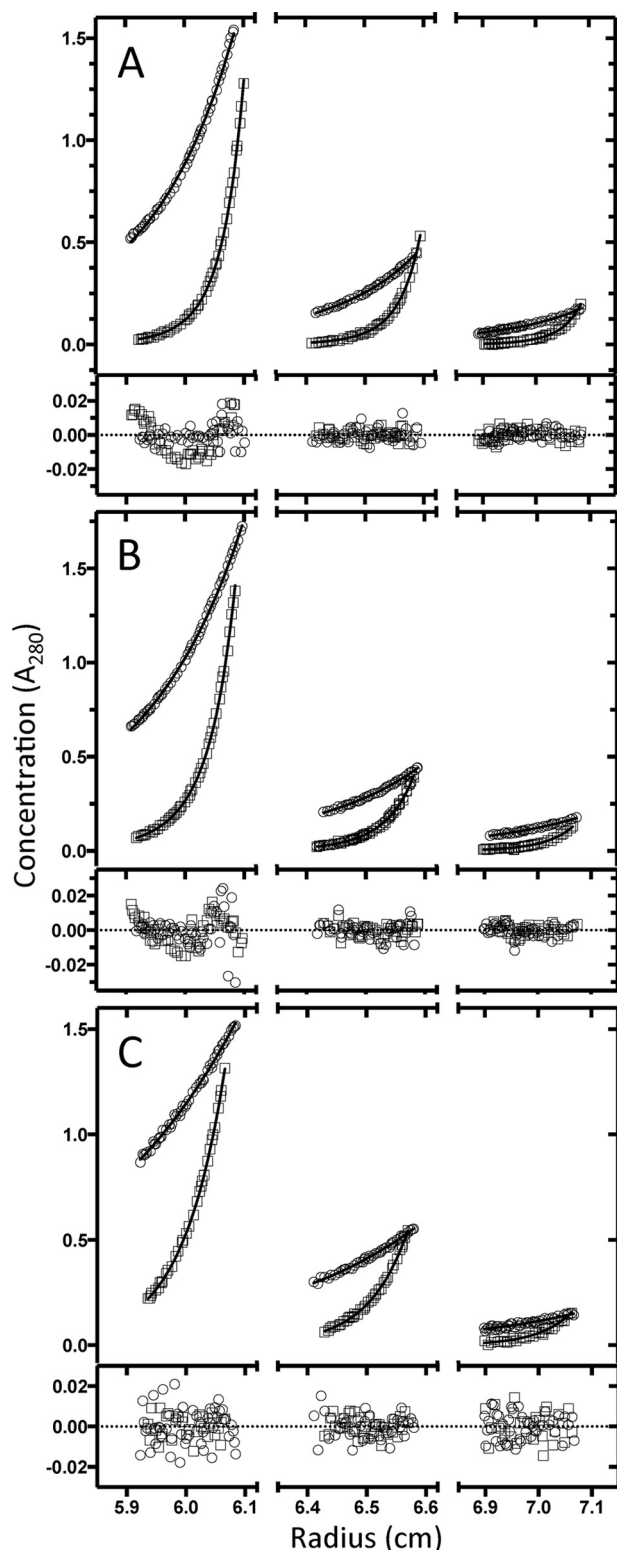
FIGURE 4. **Sedimentation equilibrium analysis of p85α at 10 °C.** The graphs show the distribution of p85α protein concentration during sedimentation equilibrium analysis at 10 °C obtained by measuring the absorption at 280 nm *versus* the radial distance from the center of the rotor. Three concentrations of full-length p85α were analyzed (1.2, 3.6, and 9.6 μM). The equilibrium protein concentration distributions measured at each of the two rotor speeds are shown (*top curve*, 8,000 rpm; *bottom curve*, 16,000 rpm) with the best global fit to a monomer-dimer association model shown as the *solid line* in 20 mM NaCl (*A*) and 500 mM NaCl (*B*) and fit to the weight average molecular weight of a single species in 500 mM NaCl in the presence of proline-rich peptide (*C*). The residuals for the fit are shown by the *symbols* along the *dotted line* at 0.0.
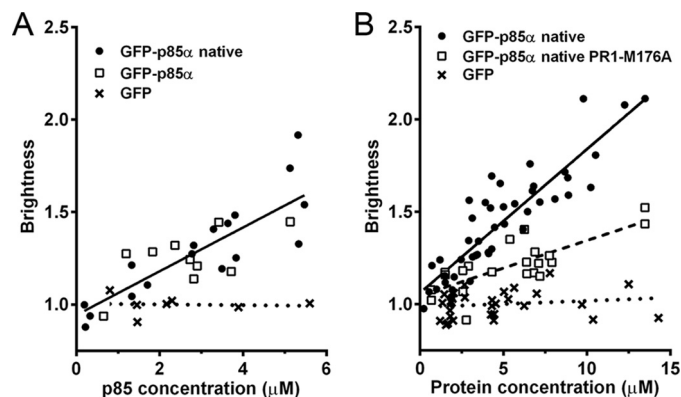

FIGURE 5. **p85α dimerization *in vivo* measured by FFS.** *A*, U2OS cells were transfected with GFP-p85α or native GFP-p85α. Brightness was measured as a function of concentration and compared with a monomeric GFP control. The data sets were not significantly different, as indicated by their common regression line. *B*, U201S cells were transfected with native GFP-p85α or native GFP-p85α PR1/M176A. Brightness was measured as a function of concentration and compared with a monomeric GFP control.

any single sampled conformational state. For example, in the best scoring single-state model (*light red* in Fig. 6B), $\chi > 13.9$, and only 48% of the DST cross-links were satisfied. This result suggests that the p85α(1–333) dimer is conformationally heterogeneous in solution.

We therefore computed multistate models of the p85α(1–333) dimer for up to 9 states, using MultiFoXS (42, 69). The results show that a weighted combination of five states is sufficient to explain the experimental dimer SAXS profile within its noise ($\chi = 2.623$; *blue* in Fig. 6B) and all of the 25 chemical cross-links within a distance threshold of 35 Å (Fig. 6D). The best scoring multistate model of the p85α(1–333) dimer consists of three major states (conformations) with population weights of 40.3% (*blue*), 27.7% (*red*), and 16.6% (*yellow*) and two minor states with population weights of 8.0% (*green*) and 7.4% (*purple*) (Fig. 6C). The maximum particle sizes (D_{max}) of the major states ranged from 145 to 185 Å. D_{max} values of the minor states are ~110 and ~250 Å. The root mean square deviation and the template modeling scores (73) for each pair of the five states range from 18.3 to 36.1 Å and from 0.55 to 0.57, respectively, indicating highly heterogeneous folds within the multistate model.

Similarly to the p85α(1–333) dimer, the full-length p85α dimer is conformationally heterogeneous in solution; neither the SAXS profile nor the cross-linking data set was simultaneously explained by any single sampled conformational state. For the best scoring single-state model (*light red* in Fig. 7B), $\chi > 1.671$, only 40% of the combined 256 DST cross-links were satisfied. We therefore computed multistate models of the p85α dimer for up to nine states, using the most populated state of the p85α(1–333) dimer (40.3%, *colored blue* in Fig. 6C) as an additional constraint in the selected restraint subsets. This model accommodates all of the SAXS and cross-linking data. The results show that a weighted combination of five states is sufficient to explain the experimental dimer SAXS profile within its noise ($\chi = 1.275$; *blue* in Fig. 7B) and 95% of the combined 256 chemical cross-links within a distance threshold of 35 Å (Fig. 7D). The best scoring multistate model of the p85α dimer consists of three major states with population weights of 33.2% (*blue*), 27.4% (*red*), and 18.2% (*yellow*) and two minor states with population weights of 13.4% (*green*) and 7.9%

TABLE 1

Summary of SAXS analysis

Table 1 summarizes SAXS parameters of molecular mass, R_g, D_{max}, and Porod volume calculated from SAXS profiles of p85α full-length and p85α(1–333) samples, under the low salt condition (20 mM NaCl) at 10°C. The SAXS parameters obtained under the conditions favoring the dimer state are highlighted in gray shading and boldface type. R_g values were calculated using DATGNOM and AUTORG in the ATSAS package (37) in real and reciprocal space, respectively. Porod volumes were calculated using DATPOROD in the ATSAS package (37). Additional tables for other SAXS samples are available on the Sali Lab p85 website.

Protein	Concentration		20mM NaCl (10°C)					Native Molecular Mass	
	(mg/mL)	(μM)	M.Mass* estimation (kDa)	D_{max} (Å)	R_g (Real) (Å)	R_g (Reciprocal) (Å)	Porod volume (Å³)	Monomer (kDa)	Dimer (kDa)
p85α	0.5 †	6.0 †	141.0	171.6	51.3	53.1 ± 3.3	259,815	84	168
	1.0	**12.0**	**176.8**	**199.1**	**59.5**	**57.7 ± 0.9**	**374,029**		
	1.5	18.0	199.0	206.6	62.7	62.8 ± 1.3	475,310		
	2.0	24.0	207.1	209.7	63.0	63.7 ± 0.7	490,793		
	5.0	60.0	289.1	232.7	70.7	70.8 ± 1.0	688,412		
p85α$^{1-333}$	0.5 †	13.3†	60.0	151.5	43.3	37.3 ± 3.3	81,499	38	75
	0.75	19.9	67.5	150.8	43.1	41.0 ± 2.0	83,867		
	1.0	26.5	69.2	154.3	44.1	43.8 ± 1.5	87,460		
	2.0	53.0	72.4	157.1	44.9	44.0 ± 1.0	91,517		
	3.5	92.8	77.5	161.2	46.3	46.3 ± 1.2	97,002		
	5.0	**132.5**	**75.9**	**155.1**	**44.3**	**44.1 ± 0.6**	**95,438**		

* Molecular masses were estimated using SAXS MOW (38) with a threshold of Q_{max} = 0.2–0.3 (1/Å), depending on the data. Native molecular masses of the p85α monomer and dimer are 84 and 168 kDa, respectively. In contrast, molecular masses of the p85α(1–333) monomer and dimer are 38 and 75 kDa, respectively.

† SAXS data has a higher noise at low concentrations (~0.5 mg/ml; gray type) than at high concentrations.

(*purple*) (Fig. 7*C*). The maximum particle sizes (D_{max}) of the five states ranged from 170 to 320 Å. The root mean square deviation and the template modeling scores (73) for each pair of the five states range from 26.8 to 65.6 Å and 0.27 to 0.43, respectively, indicating more conformational heterogeneity than the p85α(1–333) dimer.

Based on the multistate model, the conformational dynamics of the p85α(1–333) dimer appear to be dominated by the relative intramolecular motions of the SH3 and BCR domains, connected by the PR1 motif linkers (residues 85–115) (Fig. 6*C*). The maximal displacement between the SH3 and BCR domains in the multistate model is ~100 Å. Notably, the BCR domains do not appear to contact each other directly, in agreement with experimental results showing that the BCR domain is monomeric (residues 78–322; Fig. 3*A*). Reciprocal intermolecular SH3-PR1 interactions were identified in each of the five states, consistent with this interaction as a critical mediator of dimerization.

A large degree of heterogeneity is observed in the p85α dimer, particularly in the coiled-coil (iSH2) domains, as well as in the neighboring nSH2 and cSH2 domains. Importantly, the multistate model indicates that the two iSH2 domains orient relative to one another in parallel, anti-parallel, or even perpendicular orientations (Fig. 7*C*). The heterogeneity in iSH2 domain orientation is supported by LOGICOIL calculations, a coiled-coil oligomerization state prediction program (77). The configurations of the intermolecular SH3-PR1 interaction sites were in agreement with our AUC results (Fig. 3*A*). Similarly, two BCR domains were not in contact with each other, which is also consistent with the AUC data. The previously discussed contribution of the cSH2-cSH2 contacts to p85α dimerization is also seen in the multistate model (Fig. 7*C*). In conclusion, it appears that both the p85α(1–333) and full-length p85α dimers

are highly dynamic molecules in solution, held together by the SH3-PR1 and cSH2 contacts, with the maximal dimension of the molecules in solution (D_{max}) ranging from 110 to 250 Å and from 170 to 320 Å, respectively.

Discussion

The five discrete protein-binding domains of p85α allow it to function as a scaffolding protein and mediate the activity of multiple signaling pathways. Our studies explore whether the physical properties of p85α actively regulate its interactions with other signaling proteins. The fact that p85α dimerization is rapidly and freely reversible and its conformational states are highly heterogeneous would maximize its ability to interact with regulatory partners. p85α dimerization occurs *in vivo* in a concentration-dependent manner, demonstrating that the properties of p85α measured *in vitro* are relevant to those in the cell (Fig. 5). If the partners of p85α preferentially bind to the monomer or dimer, the intracellular concentration of p85α, and hence its dimerization state, could play a role in modulating the activity of its binding partners in the cell.

These studies are enabled by the design, expression, and purification of a p85α variant in which its six cysteines are mutated to residues of a similar chemical nature (*i.e.* similar degree of hydrophobicity as inferred from crystal structures). Removal of surface cysteines to stabilize protein expression and purification is a commonly used technique; exposed cysteines have pK_a values comparable with physiological pH (78) and thus are highly responsive to fluctuations in physiological and environmental conditions (79). Importantly, our cysteine-free p85α behaves identically to the native protein in all functional assays because all cysteine-free domains retain their ability to interact with known binding partners (Fig. 2). Thus, cysteine-
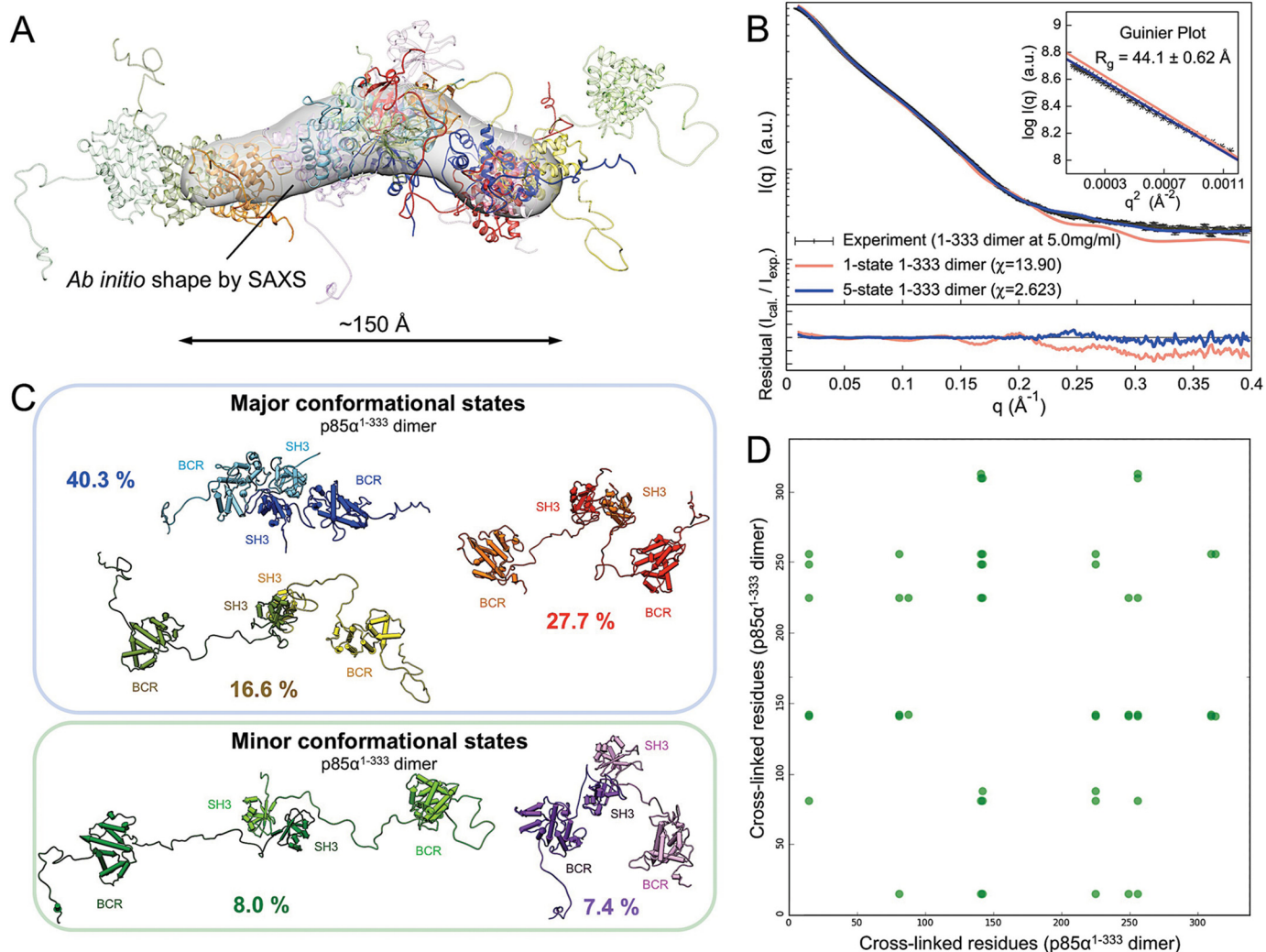
FIGURE 6. **Structure and dynamics of the p85α(1–333) homodimer revealed through an integrative modeling approach.** *A*, the best scoring multistate model is composed of three major states with population weights of 40.3% (*blue*), 27.7% (*red*), and 16.6% (*yellow*) and two minor states with population weights of 8.0% (*green*) and 7.4% (*purple*). The most populated state (*blue*) was used as a reference for rigid body least-squares superposition of the remaining four states. The *ab initio* shape (represented as a *gray envelope*) computed from the experimental SAXS profile was also superposed for comparison. *B*, comparison of the experimental SAXS profile (*black*, in arbitrary units (*a.u.*)) of the p85α(1–333) dimer with the calculated SAXS profiles from the single-state ($\chi = 13.90$, *red*) and the five-state ($\chi = 2.623$, *blue*) models. The *bottom plot* shows the residuals (calculated intensity/experimental intensity) of each calculated SAXS profile. The *top inset* shows the SAXS profiles in the Guinier plot (in arbitrary units) with an R_g fit of 44.1 ± 0.62 Å. The maximum particle size (D_{max}) was ~150 Å (determined experimentally; Table 1). *C*, each of the five states in the multistate model along with population weights and domain labels is shown. *Colors* were adjusted to distinguish individual domains in the dimer. The conformational dynamics of p85α(1–333) dimer appear to be dominated by the relative intramolecular motions of the SH3 and BCR domains, connected by the PR1 motif linkers. *D*, consistency between the 25 DST chemical cross-links and the multistate model of the p85α(1–333) dimer. The *green dots* represent cross-linked residue pairs satisfied by the multistate model within the distance threshold of 35 Å. The multistate model of the p85α(1–333) dimer satisfied all 25 DST chemical cross-links.

free p85α is a validated model for structural and biophysical analysis of the p85α protein. Moreover, this validated model will serve as a platform for selective labeling with probes in future structure and dynamics studies.

We used our understanding of the chemical nature of the self-assembly equilibrium to identify conditions under which p85α is predominantly dimeric. Using these conditions, we obtained chemical cross-linking and SAXS data that were used for integrative structure determination of the p85α dimer. The flexible, elongated shape of the p85α dimer states visualized in the multistate model (Fig. 7C) highlights the importance of using sedimentation equilibrium (13) and SAXS to determine accurate molecular weights independent of molecular shape in studies of this molecule and its complexes.

Our sedimentation equilibrium analyses underscore the importance of the previously identified intermolecular SH3-PR1 interactions (13) at physiological conditions (Fig. 3). Our studies also demonstrate novel intermolecular electrostatic interactions mediated by the cSH2 domain, which stabilize the p85α dimer. AUC, SAXS, and chemical cross-linking results all support the presence of a cSH2 dimer contact. The structural consequence of the N-terminal (SH3-PR1) and C-terminal (cSH2-cSH2) contacts is that the p85α polypeptide is essentially pinned at each end in the dimer, allowing the intervening domains to exhibit substantial conformational flexibility (Fig. 7C). The relative contribution of the SH3-PR1 and cSH2 dimer contacts to p85α dimer stability in cells deserves further study.
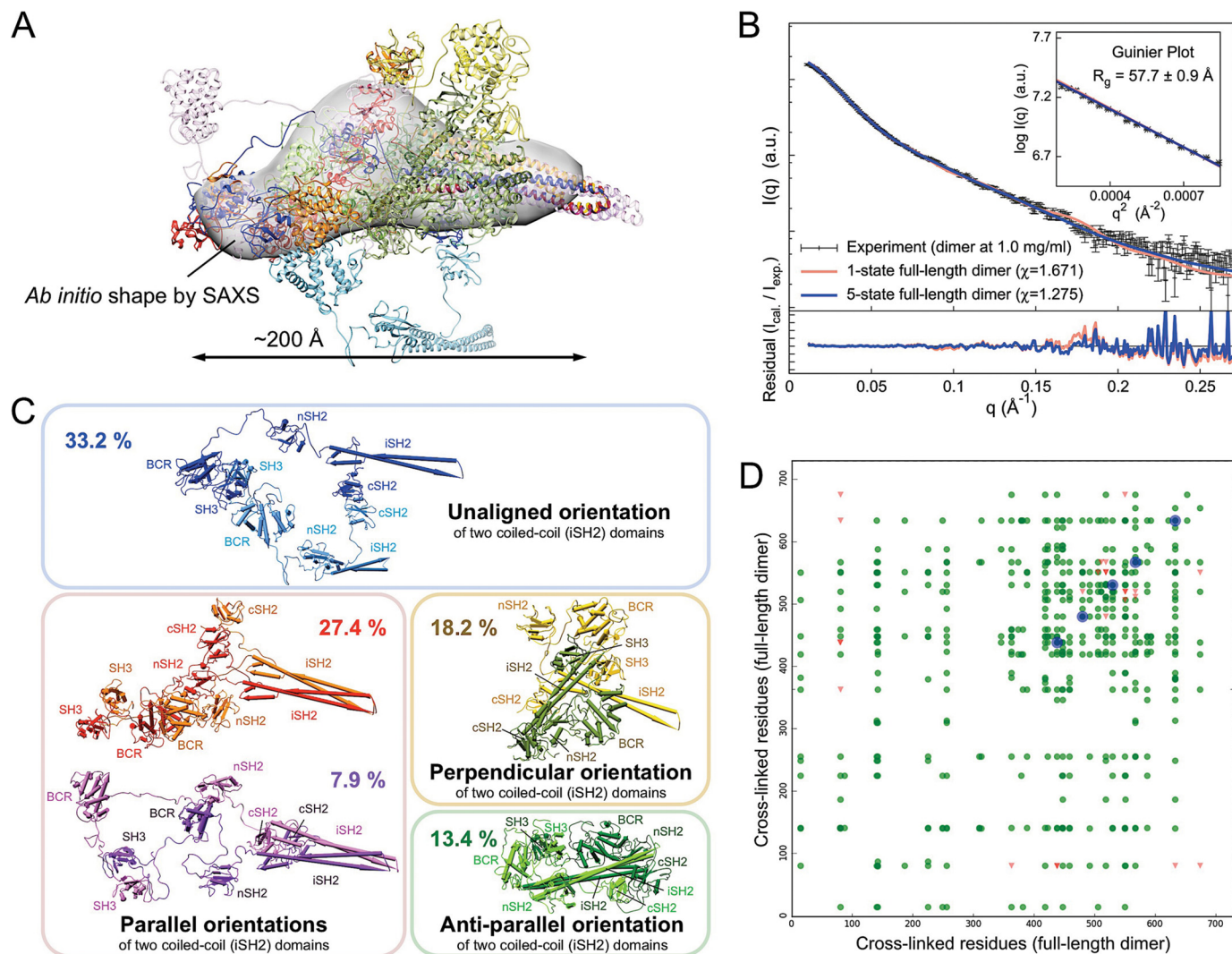
FIGURE 7. **Structure and dynamics of the full-length p85α homodimer revealed through an integrative modeling approach.** *A*, the best scoring multistate model is composed of three major states with population weights of 33.2% (*blue*), 27.4% (*red*), and 18.2% (*yellow*) and two minor states with population weights of 13.4% (*green*) and 7.9% (*purple*). The most populated state (*blue*) was used as a reference for rigid body least-squares superposition of the remaining four states. The *ab initio* shape (represented as a *gray envelope*) computed from the experimental SAXS profile was also superposed for comparison. *B*, comparison of the experimental SAXS profile (*black*, in arbitrary units (*a.u.*)) of the p85α dimer with the calculated SAXS profiles from the single-state ($\chi = 1.671$, *red*) and the five-state ($\chi = 1.275$, *blue*) models. The *bottom plot* shows the residuals (calculated intensity/experimental intensity) of each calculated SAXS profile. The *top inset* shows the SAXS profiles in the Guinier plot (in arbitrary units) with an R_g fit of 57.7 ± 0.9 Å. The maximum particle size (D_{max}) was ~200 Å (determined experimentally; Table 1). *C*, each of the five states in the multistate model, along with population weights and domain labels, is shown. *Colors* were adjusted to distinguish individual domains in the dimer. A large degree of heterogeneity was observed in the full-length p85α dimer, particularly in the coiled-coil (iSH2) domains as well as the neighboring nSH2 and cSH2 domains. The two iSH2 domains are oriented in multiple conformations relative to one another (*e.g.* parallel, anti-parallel, and perpendicular). *D*, consistency between the combined 256 (25 DST and 231 DSS) chemical cross-links and the multistate model of the full-length p85α dimer. *Green dots*, cross-linked residue pairs satisfied by the multistate model within the distance threshold of 35 Å. *Red triangles*, cross-linked residue pairs that violated the distance threshold of 35 Å. *Blue dots*, five homodimer chemical cross-links identified on the same residues between two subunits in the dimer. The multistate model of p85α dimer satisfied 244 (95%) of the combined 256 chemical cross-links.

Although crystal structures have been solved for the five individual domains of native p85α (49–51, 53, 80–84), the protein has not been amenable to either x-ray crystallography, presumably because of the protein's flexibility, or NMR spectroscopy, due to its size. The orientation and spatial relation of each domain relative to the others is unknown, although this knowledge is critically important to defining the molecular mechanism(s) of p85α-mediated regulation of PI3K signaling. Thus, we explored the structure and dynamics of the p85α dimers by applying an integrative modeling approach that relies on data from orthogonal experimental methods at different levels of resolution. The result is a multistate model of the p85α dimer that defines the conforma-

tions and populations of individual states (Figs. 6C and 7C). An important result is the conformational heterogeneity of the p85α dimer, which is evident in the structural diversity of the multiple states that comprise the multistate model.

We addressed the issue of conformational heterogeneity by first modeling the p85α(1–333) dimer because it is more amenable than p85α to chemical cross-linking experiments yet still exhibits the monomer/dimer equilibrium of the full-length protein. The multiple states of the p85α(1–333) dimer that constitute the multistate model differ in the relative orientation of the SH3 and BCR domains. Notably, the BCR domains do not directly contact each other. In the most populated (40.3%) state,

both SH3 domains interact in *trans* with the PR1 regions of the opposing p85α(1–333) fragment.

We computed the multistate model of the full-length p85α dimer using this SH3-BCR conformational state as a constraint, in conjunction with cross-linking and SAXS data. The conformational heterogeneity that characterizes the p85α dimer is mainly due to the diverse configurations of the coiled-coil (iSH2) domains as well as the neighboring nSH2 and cSH2 domains. The two iSH2 domains in the p85α dimer are oriented parallel, anti-parallel, or even perpendicularly, relative to each other. The variety of orientations identified in the multistate model is consistent with AUC data showing that the iSH2 domains do not appear to significantly stabilize the p85α dimer. This conformational flexibility may allow iSH2 to form heterologous interactions within the context of the p85α dimer. In contrast, the cSH2 domains contact each other in all five states of the multistate model, consistent with their contribution to dimerization as observed by AUC (Fig. 3*E*).

In agreement with our AUC results showing lack of BCR dimerization in solution, the BCR domains do not appear to interact with each other in the multistate model of either the p85α(1–333) or p85α dimers. Although the two BCR domains are juxtaposed within one of the five conformational states (Fig. 7*C*; 27.4%, *red* and *orange*) we have no evidence that these domains stabilize the p85α dimer (Fig. 3*A*).

A study recently published by Cheung *et al.* (85) has generated a model of the p85^SH3-BCR fragment as a dimer bound to PTEN and small GTPase Rab5. In this model, the dimer interface consists of SH3-PR1 and BCR-BCR contacts, the latter based on a previously published crystal structure of the BCR domain that shows a BCR homodimer (49). The dimerization K_d measured for their His-PR1-BCR construct is 162.9 ± 41.4 μM, indicating very weak assembly. In contrast, we did not detect any dimerization of an untagged PR1-BCR-PR2 construct (p85α(78–322)) at three temperatures and two solution conditions. Not surprisingly, the presence of SH3-binding peptide had no effect on p85α(78–322) oligomerization unlike its complete inhibition of dimerization of p85α and the deletion fragments that contain the SH3 domain. It is possible that the presence of a His tag in the constructs studied by Cheung *et al.* (85) enhanced the dimerization of the PR1-BCR fragment because purification of His-tagged proteins using nickel chromatography can result in oligomerization (68). Even if BCR-BCR contacts do weakly contribute to p85α dimer stabilization in the contact of the full-length protein, the role of contacts seen in the BCR crystal structure is uncertain. A DiMoVo score (36) of 0.366 in the published structure (PDB code 1PBW) suggests a crystallographic dimer, not a biological one. It remains possible that binding of additional partners, such as PTEN, may bring the BCR domains into closer proximity to one another and further stabilize p85α in its dimeric form.

Another issue for future work will be whether the same interactions that drive p85α homodimerization occur when p85α is bound to p110. Although there is one report of p85/p110 heterotetramers in cultured cells (63), these higher order complexes have not been reported during purification and gel filtration analysis of recombinant p85/p110 dimers. Structures of the nSH2-iSH2/p110α and iSH2-cSH2/p110β heterodimers show that the adaptor-binding domain, C2 domain, and kinase domain of p110 make extensive contacts with the iSH2 domain, whereas the nSH2 and cSH2 domains contact the helical, C2, and kinase domains (83, 84). These contacts would probably preclude a number of the conformational states derived from the SAXS and cross-linking data in this study. However, given the modest energetic contributions of the iSH2 and cSH2 domains to the formation of the p85α homodimer, it is not clear that binding of p110 to the iSH2 domain would prevent the formation of (p85/p110)$_2$ heterotetramers. Analysis of p85/p110 heterotetramers and identification of conditions that promote heterotetramer formation will be an important next step in these studies.

References

1. Backer, J. M. (2010) The regulation of class IA PI 3-kinases by inter-subunit interactions. *Curr. Top. Microbiol. Immunol.* **346,** 87–114
2. Burke, J. E., and Williams, R. L. (2015) Synergy in activating class I PI3Ks. *Trends Biochem. Sci.* **40,** 88–100
3. Maehama, T., and Dixon, J. E. (1998) The tumor suppressor, PTEN/MMAC1, dephosphorylates the lipid second messenger, phosphatidylinositol 3,4,5-trisphosphate. *J. Biol. Chem.* **273,** 13375–13378
4. Tolias, K. F., Cantley, L. C., and Carpenter, C. L. (1995) Rho family GTPases bind to phosphoinositide kinases. *J. Biol. Chem.* **270,** 17656–17659
5. Zheng, Y., Bagrodia, S., and Cerione, R. A. (1994) Activation of phosphoinositide 3-kinase activity by Cdc42Hs binding to p85. *J. Biol. Chem.* **269,** 18727–18730
6. Pleiman, C. M., Hertz, W. M., and Cambier, J. C. (1994) Activation of phosphatidylinositol-3′ kinase by Src-family kinase SH3 binding to the p85 subunit. *Science* **263,** 1609–1612
7. Hale, B. G., Batty, I. H., Downes, C. P., and Randall, R. E. (2008) Binding of influenza A virus NS1 protein to the inter-SH2 domain of p85 suggests a novel mechanism for phosphoinositide 3-kinase activation. *J. Biol. Chem.* **283,** 1372–1380
8. Park, S. W., Herrema, H., Salazar, M., Cakir, I., Cabi, S., Basibuyuk Sahin, F., Chiu, Y. H., Cantley, L. C., and Ozcan, U. (2014) BRD7 regulates XBP1's activity and glucose homeostasis through its interactions with the regulatory subunits of PI3K. *Cell Metab.* **20,** 73–84
9. Rabinovsky, R., Pochanard, P., McNear, C., Brachmann, S. M., Duke-Cohan, J. S., Garraway, L. A., and Sellers, W. R. (2009) p85 associates with unphosphorylated PTEN and the PTEN-associated complex. *Mol. Cell Biol.* **29,** 5377–5388
10. Chagpar, R. B., Links, P. H., Pastor, M. C., Furber, L. A., Hawrysh, A. D.,

Chamberlain, M. D., and Anderson, D. H. (2010) Direct positive regulation of PTEN by the p85 subunit of phosphatidylinositol 3-kinase. *Proc. Natl. Acad. Sci. U.S.A.* **107,** 5471–5476

11. Cheung, L. W., Hennessy, B. T., Li, J., Yu, S., Myers, A. P., Djordjevic, B., Lu, Y., Stemke-Hale, K., Dyer, M. D., Zhang, F., Ju, Z., Cantley, L. C., Scherer, S. E., Liang, H., Lu, K. H., Broaddus, R. R., and Mills, G. B. (2011) High frequency of PIK3R1 and PIK3R2 mutations in endometrial cancer elucidates a novel mechanism for regulation of PTEN protein stability. *Cancer Discov.* **1,** 170–185

12. Kapeller, R., Prasad, K. V., Janssen, O., Hou, W., Schaffhausen, B. S., Rudd, C. E., and Cantley, L. C. (1994) Identification of two SH3-binding motifs in the regulatory subunit of phosphatidylinositol 3-kinase. *J. Biol. Chem.* **269,** 1927–1933

13. Harpur, A. G., Layton, M. J., Das, P., Bottomley, M. J., Panayotou, G., Driscoll, P. C., and Waterfield, M. D. (1999) Intermolecular interactions of the p85α regulatory subunit of phosphatidylinositol 3-kinase. *J. Biol. Chem.* **274,** 12323–12332

14. Russel, D., Lasker, K., Webb, B., Velázquez-Muriel, J., Tjioe, E., Schneidman-Duhovny, D., Peterson, B., and Sali, A. (2012) Putting the pieces together: integrative modeling platform software for structure determination of macromolecular assemblies. *PLoS Biol.* **10,** e1001244

15. Alber, F., Dokudovskaya, S., Veenhoff, L. M., Zhang, W., Kipper, J., Devos, D., Suprapto, A., Karni-Schmidt, O., Williams, R., Chait, B. T., Rout, M. P., and Sali, A. (2007) Determining the architectures of macromolecular assemblies. *Nature* **450,** 683–694

16. Alber, F., Förster, F., Korkin, D., Topf, M., and Sali, A. (2008) Integrating diverse data for structure determination of macromolecular assemblies. *Annu. Rev. Biochem.* **77,** 443–477

17. Webb, B., Lasker, K., Schneidman-Duhovny, D., Tjioe, E., Phillips, J., Kim, S. J., Velázquez-Muriel, J., Russel, D., and Sali, A. (2011) Modeling of proteins and their assemblies with the integrative modeling platform. *Methods Mol. Biol.* **781,** 377–397

18. Ward, A. B., Sali, A., and Wilson, I. A. (2013) Biochemistry: integrative structural biology. *Science* **339,** 913–915

19. Molnar, K. S., Bonomi, M., Pellarin, R., Clinthorne, G. D., Gonzalez, G., Goldberg, S. D., Goulian, M., Sali, A., and DeGrado, W. F. (2014) Cys-scanning disulfide crosslinking and Bayesian modeling probe the transmembrane signaling mechanism of the histidine kinase, PhoQ. *Structure* **22,** 1239–1251

20. Schneidman-Duhovny, D., Pellarin, R., and Sali, A. (2014) Uncertainty in integrative structural modeling. *Curr. Opin. Struct. Biol.* **28,** 96–104

21. Fritsch, R., de Krijger, I., Fritsch, K., George, R., Reason, B., Kumar, M. S., Diefenbacher, M., Stamp, G., and Downward, J. (2013) RAS and RHO families of GTPases directly regulate distinct phosphoinositide 3-kinase isoforms. *Cell* **153,** 1050–1063

22. Yu, J., Zhang, Y., McIlroy, J., Rordorf-Nikolic, T., Orr, G. A., and Backer, J. M. (1998) Regulation of the p85/p110 phosphatidylinositol 3′-kinase: stabilization and inhibition of the p110α catalytic subunit by the p85 regulatory subunit. *Mol. Cell. Biol.* **18,** 1379–1387

23. Philo, J. S. (2006) Improved methods for fitting sedimentation coefficient distributions derived by time-derivative techniques. *Anal. Biochem.* **354,** 238–246

24. Stafford, W. F., 3rd (1992) Boundary analysis in sedimentation transport experiments: a procedure for obtaining sedimentation coefficient distributions using the time derivative of the concentration profile. *Anal. Biochem.* **203,** 295–301

25. Cole, J. L. (2004) Analysis of heterogeneous interactions. *Methods Enzymol.* **384,** 212–232

26. Cole, J. L., Lary, J. W., Moody T., and Laue, T. M. (2008) Analytical ultracentrifugation: sedimentation velocity and sedimentation equilibrium. *Methods Cell Biol.* **84,** 143–179

27. Wu, B., Chao, J. A., and Singer, R. H. (2012) Fluorescence fluctuation spectroscopy enables quantitative imaging of single mRNAs in living cells. *Biophys. J.* **102,** 2936–2944

28. Chen, Y., Wei, L. N., and Müller, J. D. (2003) Probing protein oligomerization in living cells with fluorescence fluctuation spectroscopy. *Proc. Natl. Acad. Sci. U.S.A.* **100,** 15492–15497

29. Sanchez-Andres, A., Chen, Y., and Müller, J. D. (2005) Molecular brightness determined from a generalized form of Mandel's Q-parameter. *Biophys. J.* **89,** 3531–3547

30. Shi, Y., Fernandez-Martinez, J., Tjioe, E., Pellarin, R., Kim, S. J., Williams, R., Schneidman-Duhovny, D., Sali, A., Rout, M. P., and Chait, B. T. (2014) Structural characterization by cross-linking reveals the detailed architecture of a coatomer-related heptameric module from the nuclear pore complex. *Mol. Cell. Proteomics* **13,** 2927–2943

31. Shi, Y., Pellarin, R., Fridy, P. C., Fernandez-Martinez, J., Thompson, M. K., Li, Y., Wang, Q. J., Sali, A., Rout, M. P., and Chait, B. T. (2015) A strategy for dissecting the architectures of native macromolecular assemblies. *Nat. Methods* 10.1038/nmeth.3617

32. Yang, B., Wu, Y. J., Zhu, M., Fan, S. B., Lin, J., Zhang, K., Li, S., Chi, H., Li, Y. X., Chen, H. F., Luo, S. K., Ding, Y. H., Wang, L. H., Hao, Z., Xiu, L. Y., Chen, S., Ye, K., He, S. M., and Dong, M. Q. (2012) Identification of cross-linked peptides from complex samples. *Nat. Methods* **9,** 904–906

33. Kuwamoto, S., Akiyama, S., and Fujisawa, T. (2004) Radiation damage to a protein solution, detected by synchrotron X-ray small-angle scattering: dose-related considerations and suppression by cryoprotectants. *J. Synchrotron Rad.* **11,** 462–468

34. McPhillips, T. M., McPhillips, S. E., Chiu, H. J., Cohen, A. E., Deacon, A. M., Ellis, P. J., Garman, E., Gonzalez, A., Sauter, N. K., Phizackerley, R. P., Soltis, S. M., and Kuhn, P. (2002) Blu-Ice and the distributed control system: software for data acquisition and instrument control at macromolecular crystallography beamlines. *J. Synchrotron Radiat.* **9,** 401–406

35. Martel, A., Liu, P., Weiss, T. M., Niebuhr, M., and Tsuruta, H. (2012) An integrated high-throughput data acquisition system for biological solution x-ray scattering studies. *J. Synchrotron Radiat.* **19,** 431–434

36. Bernauer, J., Bahadur, R. P., Rodier, F., Janin, J., and Poupon, A. (2008) DiMoVo: a Voronoi tessellation-based method for discriminating crystallographic and biological protein-protein interactions. *Bioinformatics* **24,** 652–658

37. Petoukhov, M. V., Franke, D., Shkumatov, A. V., Tria, G., Kikhney, A. G., Gajda, M., Gorba, C., Mertens, H. D. T., Konarev, P. V., and Svergun, D. I. (2012) New developments in the ATSAS program package for small-angle scattering data analysis. *J. Appl. Crystallogr.* **45,** 342–350

38. Fischer, H., Neto, M. D., Napolitano, H. B., Polikarpov, I., and Craievich, A. F. (2010) Determination of the molecular weight of proteins in solution from a single small-angle x-ray scattering measurement on a relative scale. *J. Appl. Crystallogr.* **43,** 101–109

39. Franke, D., and Svergun, D. I. (2009) DAMMIF, a program for rapid ab-initio shape determination in small-angle scattering. *J. Appl. Crystallogr.* **42,** 342–346

40. Svergun, D. I. (1999) Restoring low resolution structure of biological macromolecules from solution scattering using simulated annealing. *Biophys. J.* **76,** 2879–2886

41. Volkov, V. V., and Svergun, D. I. (2003) Uniqueness of ab initio shape determination in small-angle scattering. *J. Appl. Crystallogr.* **36,** 860–864

42. Carter, L., Kim, S. J., Schneidman-Duhovny, D., Stöhr, J., Poncet-Montange, G., Weiss, T. M., Tsuruta, H., Prusiner, S. B., and Sali, A. (2015) Prion protein-antibody complexes characterized by chromatography-coupled small-angle x-ray scattering. *Biophys. J.* **109,** 793–805

43. Sali, A., Berman, H. M., Schwede, T., Trewhella, J., Kleywegt, G., Burley, S. K., Markley, J., Nakamura, H., Adams, P., Bonvin, A. M., Chiu, W., Peraro, M. D., Di Maio, F., Ferrin, T. E., Grünewald, K., Gutmanas, A., Henderson, R., Hummer, G., Iwasaki, K., Johnson, G., Lawson, C. L., Meiler, J., Marti-Renom, M. A., Montelione, G. T., Nilges, M., Nussinov, R., Patwardhan, A., Rappsilber, J., Read, R. J., Saibil, H., Schröder, G. F., Schwieters, C. D., Seidel, C. A., Svergun, D., Topf, M., Ulrich, E. L., Velankar, S., and Westbrook, J. D. (2015) Outcome of the First wwPDB Hybrid/Integrative Methods Task Force Workshop. *Structure* **23,** 1156–1167

44. Pelikan, M., Hura, G. L., and Hammel, M. (2009) Structure and flexibility within proteins as identified through small angle x-ray scattering. *Gen. Physiol. Biophys.* **28,** 174–189

45. Söding, J. (2005) Protein homology detection by HMM-HMM comparison. *Bioinformatics* **21,** 951–960

46. Söding, J., Biegert, A., and Lupas, A. N. (2005) The HHpred interactive server for protein homology detection and structure prediction. *Nucleic Acids Res.* **33,** W244–W248

47. Pieper, U., Webb, B. M., Dong, G. Q., Schneidman-Duhovny, D., Fan, H., Kim, S. J., Khuri, N., Spill, Y. G., Weinkam, P., Hammel, M., Tainer, J. A., Nilges, M., and Sali, A. (2014) ModBase, a database of annotated comparative protein structure models and associated resources. *Nucleic Acids Res.* **42,** D336–D346

48. Batra-Safferling, R., Granzin, J., Mödder, S., Hoffmann, S., and Willbold, D. (2010) Structural studies of the phosphatidylinositol 3-kinase (PI3K) SH3 domain in complex with a peptide ligand: role of the anchor residue in ligand binding. *Biol. Chem.* **391,** 33–42

49. Musacchio, A., Cantley, L. C., and Harrison, S. C. (1996) Crystal structure of the breakpoint cluster region-homology domain from phosphoinositide 3-kinase p85 α subunit. *Proc. Natl. Acad. Sci. U.S.A.* **93,** 14373–14378

50. Nolte, R. T., Eck, M. J., Schlessinger, J., Shoelson, S. E., and Harrison, S. C. (1996) Crystal structure of the PI 3-kinase p85 amino-terminal SH2 domain and its phosphopeptide complexes. *Nat. Struct. Biol.* **3,** 364–374

51. Mandelker, D., Gabelli, S. B., Schmidt-Kittler, O., Zhu, J., Cheong, I., Huang, C. H., Kinzler, K. W., Vogelstein, B., and Amzel, L. M. (2009) A frequent kinase domain mutation that changes the interaction between PI3Kα and the membrane. *Proc. Natl. Acad. Sci. U.S.A.* **106,** 16996–17001

52. Hersleth, H. P., Hsiao, Y. W., Ryde, U., Görbitz, C. H., and Andersson, K. K. (2008) The crystal structure of peroxymyoglobin generated through cryo-radiolytic reduction of myoglobin compound III during data collection. *Biochem. J.* **412,** 257–264

53. Pauptit, R. A., Dennis, C. A., Derbyshire, D. J., Breeze, A. L., Weston, S. A., Rowsell, S., and Murshudov, G. N. (2001) NMR trial models: experiences with the colicin immunity protein Im7 and the p85α C-terminal SH2-peptide complex. *Acta Crystallogr. D Biol. Crystallogr.* **57,** 1397–1404

54. Feng, S., Chen, J. K., Yu, H., Simon, J. A., and Schreiber, S. L. (1994) Two binding orientations for peptides to the Src SH3 domain: development of a general model for SH3-ligand interactions. *Science* **266,** 1241–1247

55. Zhang, X., Vadas, O., Perisic, O., Anderson, K. E., Clark, J., Hawkins, P. T., Stephens, L. R., and Williams, R. L. (2011) Structure of lipid kinase p110β/p85β elucidates an unusual SH2-domain-mediated inhibitory mechanism. *Mol. Cell* **41,** 567–578

56. Marsden, R. L., McGuffin, L. J., and Jones, D. T. (2002) Rapid protein domain assignment from amino acid sequence using predicted secondary structure. *Protein Sci.* **11,** 2814–2824

57. Jones, D. T. (1999) Protein secondary structure prediction based on position-specific scoring matrices. *J. Mol. Biol.* **292,** 195–202

58. Buchan, D. W., Minneci, F., Nugent, T. C., Bryson, K., and Jones, D. T. (2013) Scalable web services for the PSIPRED Protein Analysis Workbench. *Nucleic Acids Res.* **41,** W349–W357

59. Ward, J. J., McGuffin, L. J., Bryson, K., Buxton, B. F., and Jones, D. T. (2004) The DISOPRED server for the prediction of protein disorder. *Bioinformatics* **20,** 2138–2139

60. Sali, A., and Blundell, T. L. (1993) Comparative protein modelling by satisfaction of spatial restraints. *J. Mol. Biol.* **234,** 779–815

61. Schneidman-Duhovny, D., Hammel, M., and Sali, A. (2010) FoXS: a web server for rapid computation and fitting of SAXS profiles. *Nucleic Acids Res.* **38,** W540–W544

62. Schneidman-Duhovny, D., Hammel, M., Tainer, J. A., and Sali, A. (2013) Accurate SAXS profile computation and its assessment by contrast variation experiments. *Biophys. J.* **105,** 962–974

63. Pérez-Garcia, V., Redondo-Muñoz, J., Kumar, A., and Carrera, A. C. (2014) Cell activation-induced phosphoinositide 3-kinase α/β dimerization regulates PTEN activity. *Mol. Cell. Biol.* **34,** 3359–3373

64. Erzberger, J. P., Stengel, F., Pellarin, R., Zhang, S., Schaefer, T., Aylett, C. H., Cimermančič, P., Boehringer, D., Sali, A., Aebersold, R., and Ban, N. (2014) Molecular architecture of the 40S-eIF1-eIF3 translation initiation complex. *Cell* **158,** 1123–1135

65. Shen, M. Y., and Sali, A. (2006) Statistical potential for assessment and prediction of protein structures. *Protein Sci.* **15,** 2507–2524

66. Fernandez-Martinez, J., Phillips, J., Sekedat, M. D., Diaz-Avalos, R., Velazquez-Muriel, J., Franke, J. D., Williams, R., Stokes, D. L., Chait, B. T., Sali, A., and Rout, M. P. (2012) Structure-function mapping of a heptameric module in the nuclear pore complex. *J. Cell Biol.* **196,** 419–434

67. Rieping, W., Habeck, M., and Nilges, M. (2005) Inferential structure determination. *Science* **309,** 303–306

68. Sprules, T., Green, N., Featherstone, M., and Gehring, K. (1998) Nickel-induced oligomerization of proteins containing 10-histidine tags. *BioTechniques* **25,** 20–22

69. Lawler, E. L., and Wood, D. E. (1966) Branch-and-bound methods: a survey. *Operations Res.* **14,** 699–719

70. Kim, S. J., Fernandez-Martinez, J., Sampathkumar, P., Martel, A., Matsui, T., Tsuruta, H., Weiss, T. M., Shi, Y., Markina-Inarrairaegui, A., Bonanno, J. B., Sauder, J. M., Burley, S. K., Chait, B. T., Almo, S. C., Rout, M. P., and Sali, A. (2014) Integrative structure-function mapping of the nucleoporin Nup133 suggests a conserved mechanism for membrane anchoring of the nuclear pore complex. *Mol. Cell. Proteomics* **13,** 2911–2926

71. Rotkiewicz, P., and Skolnick, J. (2008) Fast procedure for reconstruction of full-atom protein models from reduced representations. *J. Comput. Chem.* **29,** 1460–1465

72. Pettersen, E. F., Goddard, T. D., Huang, C. C., Couch, G. S., Greenblatt, D. M., Meng, E. C., and Ferrin, T. E. (2004) UCSF Chimera: a visualization system for exploratory research and analysis. *J. Comput. Chem.* **25,** 1605–1612

73. Zhang, Y., and Skolnick, J. (2004) Scoring function for automated assessment of protein structure template quality. *Proteins* **57,** 702–710

74. Fu, Z., Aronoff-Spencer, E., Backer, J. M., and Gerfen, G. J. (2003) The structure of the inter-SH2 domain of class IA phosphoinositide 3-kinase determined by site-directed spin labeling EPR and homology modeling. *Proc. Natl. Acad. Sci. U.S.A.* **100,** 3275–3280

75. Yu, H., Chen, J. K., Feng, S., Dalgarno, D. C., Brauer, A. W., and Schreiber, S. L. (1994) Structural basis for the binding of proline-rich peptides to SH3 domains. *Cell* **76,** 933–945

76. Schneidman-Duhovny, D., Kim, S. J., and Sali, A. (2012) Integrative structural modeling with small angle x-ray scattering profiles. *BMC Struct. Biol.* **12,** 17

77. Vincent, T. L., Green, P. J., and Woolfson, D. N. (2013) LOGICOIL: multi-state prediction of coiled-coil oligomeric state. *Bioinformatics* **29,** 69–76

78. Marino, S. M., and Gladyshev, V. N. (2010) Cysteine function governs its conservation and degeneration and restricts its utilization on protein surfaces. *J. Mol. Biol.* **404,** 902–916

79. Marino, S. M., and Gladyshev, V. N. (2012) Analysis and functional prediction of reactive cysteine residues. *J. Biol. Chem.* **287,** 4419–4425

80. Koyama, S., Yu, H., Dalgarno, D. C., Shin, T. B., Zydowsky, L. D., and Schreiber, S. L. (1993) Structure of the PI3K SH3 domain and analysis of the SH3 family. *Cell* **72,** 945–952

81. Hoedemaeker, F. J., Siegal, G., Roe, S. M., Driscoll, P. C., and Abrahams, J. P. (1999) Crystal structure of the C-terminal SH2 domain of the p85α regulatory subunit of phosphoinositide 3-kinase: an SH2 domain mimicking its own substrate. *J. Mol. Biol.* **292,** 763–770

82. Booker, G. W., Breeze, A. L., Downing, A. K., Panayotou, G., Gout, I., Waterfield, M. D., and Campbell, I. D. (1992) Structure of an SH2 domain of the p85 α subunit of phosphatidylinositol-3-OH kinase. *Nature* **358,** 684–687

83. Huang, C. H., Mandelker, D., Schmidt-Kittler, O., Samuels, Y., Velculescu, V. E., Kinzler, K. W., Vogelstein, B., Gabelli, S. B., and Amzel, L. M. (2007) The structure of a human p110α/p85α complex elucidates the effects of oncogenic PI3Kα mutations. *Science* **318,** 1744–1748

84. Miled, N., Yan, Y., Hon, W. C., Perisic, O., Zvelebil, M., Inbar, Y., Schneidman-Duhovny, D., Wolfson, H. J., Backer, J. M., and Williams, R. L. (2007) Mechanism of two classes of cancer mutations in the phosphoinositide 3-kinase catalytic subunit. *Science* **317,** 239–242

85. Cheung, L. W., Walkiewicz, K. W., Besong, T. M., Guo, H., Hawke, D. H., Arold, S. T., and Mills, G. B. (2015) Regulation of the PI3K pathway through a p85α monomer-homodimer equilibrium. *Elife* **4,** e06866

86. Shi, Y., Pellarin, R., Fridy, P. C., Fernandez-Martinez, J., Thompson, M. K., Li, Y., Wang, Q. J., Sali, A., Rout, M. P., and Chait, B. T. (2015) A strategy for dissecting the architectures of native macromolecular assemblies. *Nat. Methods.* 10.1038/nmeth.3617

Assembly and Molecular Architecture of the Phosphoinositide 3-Kinase p85α Homodimer

Jaclyn LoPiccolo, Seung Joong Kim, Yi Shi, Bin Wu, Haiyan Wu, Brian T. Chait, Robert H. Singer, Andrej Sali, Michael Brenowitz, Anne R. Bresnick and Jonathan M. Backer

---